AIAA JOURNAL
Vol. 49, No. 4, April 2011

Implicit Time Spectral Method for Periodic Incompressible Flows

S. Antheaume* and C. Corre†
Domaine Universitaire, 38041 Grenoble Cedex 9, France

DOI: 10.2514/1.J050785

The time spectral method converts a time-periodic flow computation into the solution of $2N + 1$ coupled steady computations, where N denotes the number of harmonics retained in the Fourier analysis of the flow. The efficiency of the method has been previously demonstrated by several authors for compressible flow applications on structured grids using implicit solution of the large-scale steady system introduced by the coupling. In this paper, the time spectral method is extended to periodic incompressible viscous flows using a finite volume formulation of the artificial compressibility system on general moving unstructured grids. Numerical simulations of low-Reynolds flows over an airfoil show the time spectral method can afford, though not systematically, a reduction by a factor up to 5 of the computational cost with respect to a conventional unsteady technique, which computes the whole transient flow behavior.

Nomenclature

$\boldsymbol{A}, \boldsymbol{B}, \boldsymbol{J}$	=	flux Jacobian matrices
C_p	=	pressure coefficient
C_X, C_Y	=	force coefficients
c	=	airfoil chord
$\boldsymbol{F}$	=	physical flux
f^*	=	nondimensional frequency, fc/U_∞
H_0	=	heaving amplitude
$\mathcal{H}$	=	numerical flux
N	=	number of harmonics
Re	=	Reynolds number
$\mathcal{R}$	=	residual vector discretizing the flux balance
s	=	grid velocity vector
t, τ	=	physical and dual time
w	=	conservative variable vector
x	=	grid position vector
β	=	artificial compressibility parameter
η	=	global cost ratio
θ, θ_0	=	angular position and pitching amplitude
ω	=	angular velocity

Subscripts

i	=	cell index
n	=	time spectral method nth time instant
∞	=	freestream value

Superscripts

l	=	Jacobi iteration counter
m	=	dual-time counter
n	=	physical time counter

I. Introduction

THE design of aerodynamic or hydrodynamic devices often requires the study of unsteady flow configurations. When this design process is performed with numerical tools, the so called dual-time approach represents a well-established way to efficiently compute unsteady flows. In this approach the unsteady field at each step of the physical time-marching procedure is obtained as a steady solution with respect to a dual time step (DTS) [1,2]. This DTS strategy can also be viewed as finding the solution of the steady (with respect to the dual time) governing equations of the flow augmented by a source term corresponding to the discretization of the physical time derivative using typically a second-order backward difference formula (BDF). The numerical methods previously available for steady flows can be readily extended to handle unsteady flows by simply taking into account this source term. Among the many industrial flow applications requiring unsteady flow analysis, a large set of problems involve time periodicity such as helicopter rotors, wind turbines, flapping-wing propulsion mechanisms as far as external aerodynamics is concerned but also internal flows within rotor–stator combinations in the context of turbomachinery applications. A drawback of the BDF–DTS method for such flows is that it requires to compute, typically from an initial rest configuration, the whole transient of the flow before the periodic flow of interest becomes established. This flaw of the conventional dual-time strategy motivated the development of numerical methods looking directly for the periodic solution of the flow. Taking advantage of the development of the periodic flow solution into a Fourier series, Hall et al. [3] introduced an efficient method dedicated to time-periodic flows for turbomachinery applications. Following a similar line of thought, Gopinath and Jameson proposed the time spectral method (TSM) for external aerodynamics applications [4]. The TSM method transforms the original system of $(2 + d)$ unsteady equations describing the d-dimensional compressible flowfield at each time moment (two scalar equations expressing mass and energy conservation and d scalar equations expressing the conservation of the d momentum components) into an extended set of $(2N + 1) \times (d + 2)$ equations corresponding to the flow solution at $(2N + 1)$ time moments in the flow period, selected so as to ensure spectral accuracy for the physical time derivative. To make the method truly attractive, it is of course crucial to efficiently compute the steady state of this extended system of conservation laws. Since, as pointed out by [5], the explicit time integration of the TSM system displays severe stability limits when the number of harmonics N increases, several authors [6–8] have put forward implicit solution strategies. These allow the use of both large Courant–Friedrichs–Lewy (CFL) numbers ensuring faster convergence to a steady state and a high number of harmonics N that might be needed to accurately described complex unsteady flows. Up to now, TSM has been used for a wide range of applications dealing mostly with compressible flows: turbomachinery [9], rotorcraft [10]. The context of the present study is the HARVEST industrial/academic joint project devoted to the development of a cross flow water turbine technology allowing to harness the kinetic energy of rivers and oceans streams [11]. The hydrodynamic design of the turbine is currently performed using both an experimental and numerical strategy. The final objective of the present work is to improve the efficiency of the numerical design by replacing the current BDF computations of turbulent flows over

Received 22 July 2010; revision received 11 October 2010; accepted for publication 18 November 2010.

*Ph.D. Candidate, Laboratoire des Ecoulements Geophysiques et Industriels, BP 53.

†Professor, Laboratoire des Ecoulements Geophysiques et Industriels, BP 53.

sea turbine configurations [12] with a TSM approach. This supposes to adapt the TSM strategy to an incompressible flow solver. A first attempt in this direction has been recently performed by Jameson [13] using an artificial compressibility (AC) method but stability concerns emerged when computing high-frequency pitching airfoils. In the present paper, an implicit TSM strategy is successfully applied to the computation of two-dimensional incompressible laminar flow over oscillating airfoils in pitching and heaving motion recently studied in [14] using a conventional BDF method. Such two-dimensional laminar configurations represent only a first step towards the computation of more realistic three-dimensional turbulent flows over water turbines; they were, however, retained at this stage because their limited cost allows an in-depth assessment of the TSM approach proposed in the present work to speed up the integration of periodic low-speed flows. This approach relies on the AC method to describe the incompressible flow and an arbitrary Lagrangian Eulerian (ALE) strategy to describe the motion of the unstructured computational grids. It is compared with a conventional BDF approach, also combining AC and ALE, both from the viewpoint of accuracy and efficiency. The paper is organized as follows: Sec. II reviews the main ingredients of the DTS–BDF incompressible flow solver (AC model, ALE formulation, implicit time integration) and displays validation results obtained for flows over a pitching and heaving NACA0015 airfoil recently computed and analyzed by Kinsey and Dumas [14]; Sec. III details the application of TSM to the AC method, and Sec. IV describes the adaptation of an implicit treatment developed in [15] to the TSM system; in Sec. V, the implicit TSM approach is applied to the flow computation of a pitching and heaving NACA0015 airfoil for an increasing number of harmonics N in order to determine the best tradeoff between accuracy and cost (both increasing functions of N) and check whether TSM can outperform BDF. Conclusions and perspectives are drawn in the last section.

II. Incompressible Flow Solver

A. Governing Equations

The solution of the incompressible Navier–Stokes equations is typically obtained using either a pressure-based method where pressure and velocity are solved in an iterative fashion through a pressure-correction equation, or a density-based method, such as the AC approach of Chorin [16]. The latter AC strategy has been favored in this work to take advantage of efficient implicit methods previously developed for solving hyperbolic problems [15] and easy to adapt to the AC system. Let us recall the AC method provides a time-accurate solution of the one-dimensional Euler equations by finding the steady state of the following hyperbolic system of conservation laws with respect to the dual or fictitious time τ:

$$\frac{\partial}{\partial\tau}\underbrace{\begin{pmatrix} p \\ u \end{pmatrix}}_{=\boldsymbol{w}} + \underbrace{\begin{pmatrix} 0 & 0 \\ 0 & 1 \end{pmatrix}}_{=\boldsymbol{K}} \cdot \frac{\partial}{\partial t}\begin{pmatrix} p \\ u \end{pmatrix} + \frac{\partial}{\partial x}\underbrace{\begin{pmatrix} \beta u \\ u^2 + p \end{pmatrix}}_{=f(\boldsymbol{w};\beta)} = 0 \qquad (1)$$

with x the space variable, t the physical time, p, u the pressure and velocity, β the constant AC parameter. At steady state on τ, the solution $u(x,t)$ of Eq. (1) satisfies the zero-divergence condition while both fields $u(x,t)$ and $p(x,t)$ satisfy the unsteady (with respect to t) momentum equation. Rewriting Eq. (1) in the compact form of a one-dimensional hyperbolic system with a source term:

$$\frac{\partial \boldsymbol{w}}{\partial\tau} + \frac{\partial}{\partial x}\boldsymbol{f}(\boldsymbol{w};\beta) = \boldsymbol{S} = -\boldsymbol{K}\frac{\partial \boldsymbol{w}}{\partial t}$$

makes clear the AC system can be efficiently driven to an accurate steady solution by making use of tools initially developed in the context of compressible flow solutions: second-order upwind discretization for the flux derivative, second-order BDF discretization for the physical time derivative and first-order implicit stage for fast convergence on the dual time. Note the choice of value for the AC parameter β affects the overall convergence rate as well as the accuracy of the physical solution through the numerical dissipation of the space discretization; however, as long as the steady state on τ is correctly achieved, the AC system remains consistent with the incompressible flow equations whatever the value of β. Let us now turn to the AC system extended to the case of two-dimensional incompressible viscous flows computed on moving grids. Let $\Omega(t) \subset \Re^2$ be an arbitrary control surface bounded by a smooth closed contour $\partial\Omega(t)$ which moves independently from the flow with a velocity $\boldsymbol{s}(\boldsymbol{x},t) = s_x(t)\boldsymbol{i} + s_y(t)\boldsymbol{j}$, where $\boldsymbol{x} = x\boldsymbol{i} + y\boldsymbol{j}$ denotes the vector of Cartesian coordinates in the absolute frame of reference. In the ALE framework, the two-dimensional Navier–Stokes equations for incompressible unsteady flows, modified to account for the AC method, can be expressed in the following integral form:

$$\frac{\partial}{\partial\tau}\int_{\Omega(t)} \boldsymbol{w}\,\mathrm{d}\Omega(t) + \boldsymbol{K}\frac{\partial}{\partial t}\int_{\Omega(t)} \boldsymbol{w}\,\mathrm{d}\Omega(t) + \int_{\partial\Omega(t)} (\boldsymbol{F}^E - \boldsymbol{F}^V)\cdot\boldsymbol{n}\,\mathrm{d}\gamma(t) = 0 \qquad (2)$$

where $\boldsymbol{n}$ is the outward unit normal vector and γ the curvilinear abscissa of $\partial\Omega$. The vector of conservative variables $\boldsymbol{w}$, the singular matrix $\boldsymbol{K}$, the inviscid fluxes $\boldsymbol{F}^E = (\boldsymbol{f}^E, \boldsymbol{g}^E)$ and the viscous fluxes $\boldsymbol{F}^V = (\boldsymbol{f}^V, \boldsymbol{g}^V)$ are defined by

$$\boldsymbol{w} = \begin{pmatrix} p \\ u \\ v \end{pmatrix}, \qquad \boldsymbol{K} = \begin{pmatrix} 0 & 0 & 0 \\ 0 & 1 & 0 \\ 0 & 0 & 1 \end{pmatrix}$$

$$\boldsymbol{f}^E(\boldsymbol{w}) = \begin{pmatrix} \beta(u - s_x) \\ u(u - s_x) + p \\ v(u - s_x) \end{pmatrix}, \qquad \boldsymbol{g}^E(\boldsymbol{w}) = \begin{pmatrix} \beta(v - s_y) \\ u(v - s_y) \\ v(v - s_y) + p \end{pmatrix}$$

$$\boldsymbol{f}^V\left(\frac{\partial \boldsymbol{w}}{\partial x}, \frac{\partial \boldsymbol{w}}{\partial y}\right) = \frac{1}{Re}\begin{pmatrix} 0 \\ 2\frac{\partial u}{\partial x} \\ \frac{\partial u}{\partial y} + \frac{\partial v}{\partial x} \end{pmatrix}$$

$$\boldsymbol{g}^V\left(\frac{\partial \boldsymbol{w}}{\partial x}, \frac{\partial \boldsymbol{w}}{\partial y}\right) = \frac{1}{Re}\begin{pmatrix} 0 \\ \frac{\partial u}{\partial y} + \frac{\partial v}{\partial x} \\ 2\frac{\partial v}{\partial y} \end{pmatrix}$$

The pressure p and the components (u, v) of the fluid velocity in the absolute frame of reference are normalized, respectively, by $\rho_\infty U_\infty^2$ and U_∞, with ρ_∞ and U_∞ the freestream density and velocity magnitude. For the following airfoil flow computations, the Reynolds number $Re = \rho_\infty U_\infty c/\mu_\infty$ is based on the airfoil chord c. The next subsection describes the finite volume upwind scheme and implicit time discretization used in this work to solve the so called ALE–AC system (2).

B. Numerical Methods

1. Spatial Discretization

System (2) is solved on general unstructured grids using a finite volume approach. Applying system (2) on a given cell Ω_i, introducing the average value $\bar{\boldsymbol{w}}$ of $\boldsymbol{w}$ over the cell and decomposing the flux balance as the sum of fluxes through each face $\Gamma_{i,k}$ of cell Ω_i leads to

$$\frac{\partial}{\partial\tau}(\bar{\boldsymbol{w}}_i|\Omega_i|) + \boldsymbol{K}\frac{\partial}{\partial t}(\bar{\boldsymbol{w}}_i|\Omega_i|) + \sum_k \int_{\Gamma_{i,k}} (\boldsymbol{F}^E - \boldsymbol{F}^V)\cdot\boldsymbol{n}\,\mathrm{d}\gamma = 0 \qquad (3)$$

where $|\Omega_i|$ is the surface of the ith grid cell Ω_i. The normal physical flux vector $(\boldsymbol{F}^E - \boldsymbol{F}^V)\cdot\boldsymbol{n}$ through the face $\Gamma_{i,k}$ of length $|\Gamma_{i,k}|$ is approximated by the numerical flux vector $\mathcal{H} = \mathcal{H}^E - \mathcal{H}^V$ computed at the center i, k of the face $\Gamma_{i,k}$:

$$\int_{\Gamma_{i,k}} (\boldsymbol{F}^E - \boldsymbol{F}^V)\cdot\boldsymbol{n}\,\mathrm{d}\gamma = (\mathcal{H}^E_{i,k} - \mathcal{H}^V_{i,k})|\Gamma_{i,k}| + O(h^p)$$

where h denotes a typical grid length. The space accuracy order p will depend on the choice of polynomial reconstruction used for the

conservative variable inside each grid cell; a linear reconstruction will be systematically used in this work leading to second-order accuracy in space. For this reason and without loss of accuracy, the average state in cell i is replaced by the state at cell center, denoted $\boldsymbol{w}_i$ from now on. The Roe approximate Riemann solver initially developed to solve the compressible Euler equations [17] is adapted to the hyperbolic ALE–AC system (2) and combined with a MUSCL variable reconstruction approach [18,19] in order to derive the inviscid numerical flux formula $\mathcal{H}^E_{i,k}$:

$$\mathcal{H}^{E}_{i,k} = \frac{1}{2}(\boldsymbol{F}^E(w^L_k)\cdot\boldsymbol{n}_{i,k} + \boldsymbol{F}^E(w^R_k)\cdot\boldsymbol{n}_{i,k}) + \frac{1}{2}\boldsymbol{Q}^E_{i,k}(\boldsymbol{w}^L_k - \boldsymbol{w}^R_k) \quad (4)$$

where $\boldsymbol{w}^{L/R}$ are the reconstructed states, respectively, on the left and right side of the kth interface $\Gamma_{i,k}$ of cell Ω_i, $\boldsymbol{Q}^E$ is the Roe numerical dissipation matrix. The states at face center i, k are linearly reconstructed from the cell center values in the cells i and $o(i,k)$ sharing the face $\Gamma_{i,k}$ and the cell gradients $\nabla\boldsymbol{w}$ in each of these cells:

$$\begin{cases} \boldsymbol{w}^L_k = \boldsymbol{w}_i + \nabla\boldsymbol{w}_i\cdot\boldsymbol{r}_{i,k} \\ \boldsymbol{w}^R_k = \boldsymbol{w}_{o(i,k)} + \nabla\boldsymbol{w}_{o(i,k)}\cdot\boldsymbol{r}_{o(i,k)} \end{cases} \quad (5)$$

where $\boldsymbol{r}_{i,k}$ (respectively $\boldsymbol{r}_{o(i,k)}$) denotes the vector extending from the cell center i (respectively $o(i,k)$) to the center of the interface $\Gamma_{i,k}$. The gradient $\nabla\boldsymbol{w}_i$ is computed at each cell center i using a least-square formula applied on a fixed spatial support including the neighboring cells sharing at least a node with cell i [19]. The Roe numerical dissipation matrix $\boldsymbol{Q}^E$ is given by

$$\boldsymbol{Q}^E = |\boldsymbol{A}^E n_x + \boldsymbol{B}^E n_y| = |\boldsymbol{J}^E_\perp|$$

where $\boldsymbol{n} = (n_x, n_y)$ and $\boldsymbol{A}^E$, $\boldsymbol{B}^E$ are the inviscid flux Jacobian matrices: $\boldsymbol{A}^E = d\boldsymbol{f}^E/d\boldsymbol{w}$, $\boldsymbol{B}^E = d\boldsymbol{g}^E/d\boldsymbol{w}$. An immediate calculation for system (2) yields

$$\boldsymbol{J}^E_\perp = \begin{pmatrix} 0 & \beta n_x & \beta n_y \\ n_x & V_\perp - s_\perp + u n_x & u n_y \\ n_y & v n_x & V_\perp - s_\perp + v n_y \end{pmatrix}$$

where $V_\perp = u n_x + v n_y$, $s_\perp = s_x n_x + s_y n_y$. This Jacobian matrix can be also expressed as $\boldsymbol{J}^E_\perp = \boldsymbol{T}|\boldsymbol{\Lambda}^E|\boldsymbol{T}^{-1}$ with $\boldsymbol{\Lambda}^E$ the diagonal matrix containing the real eigenvalues of the hyperbolic system (2). The Roe dissipation matrix is eventually computed as

$$\boldsymbol{Q}^E_{i,k} = \boldsymbol{T}_{i,k}|\boldsymbol{\Lambda}^E_{i,k}|\boldsymbol{T}^{-1}_{i,k}$$

with the state $\boldsymbol{w}_{i,k}$ taken as the arithmetic average of $\boldsymbol{w}^L_{i,k}$, $\boldsymbol{w}^R_{i,k}$ following Taylor and Whitfield [20]. The viscous fluxes are approximated using a linearly exact extension of the diamond method of Noh [21], not detailed here. Let us point out the steady state of system (2) depends on the AC parameter β through the numerical dissipation matrix $\boldsymbol{Q}^E$. The numerical inviscid flux balance or residual will be denoted thus, from now on:

$$\mathcal{R}^E_i(\boldsymbol{w},\boldsymbol{x},\boldsymbol{s}) = \frac{1}{|\Omega_i|}\sum_k \mathcal{H}^E_{i,k}|\Gamma_{i,k}| \quad (6)$$

where, in the context of the ALE formulation, the dependence of this flux balance on the mesh position $\boldsymbol{x}$ and speed $\boldsymbol{s}$ has been made explicit. Similarly, the viscous flux balance or residual will be denoted

$$\mathcal{R}^V_i(\boldsymbol{w},\boldsymbol{x}) = \frac{1}{|\Omega_i|}\sum_k \mathcal{H}^V_{i,k}|\Gamma_{i,k}| \quad (7)$$

with an explicit dependence on the grid position $\boldsymbol{x}$. Since only rigid body motion is considered for the moving grid computation performed in the present work, the cell surface $|\Omega_i|$ will remain constant over time and can be removed from the dual and physical time derivatives in Eq. (3) to be inserted into the inviscid and viscous residual Eqs. (6) and (7). The semidiscrete form of Eq. (3) of the ALE–AC system can also be expressed as

$$\frac{\partial\boldsymbol{w}_i}{\partial\tau_i} + \boldsymbol{K}\frac{\partial\boldsymbol{w}_i}{\partial t} + \mathcal{R}^E_i(\boldsymbol{w},\boldsymbol{x},\boldsymbol{s}) = \mathcal{R}^V_i(\boldsymbol{w},\boldsymbol{x}) \quad (8)$$

2. Time Discretization Including ALE Treatment

When dealing with moving airfoils in the ALE reference frame, two main approaches can be considered for taking into account the grid motion. The first approach is the rigid body technique in which all grid points have the same motion as the airfoil. The initial quality of the mesh is preserved but unsteady boundary conditions must be implemented that include the grid velocities. A drawback of this approach is that, for high-frequency pitching movements, relative velocity of in cells away from the center of rotation may become very large leading to excessive numerical dissipation. The second approach deforms the inner cells of the grid to conform to the instantaneous position of the airfoil while the outer boundaries are kept fixed. Deformation can be performed using methods based on spring analogy, which involve either the solution of a large system of equations for the displacements of nodes [22,23] and/or a local remeshing at each physical time step of the calculation [24,25]. In all these methods, a geometric conservation law must also be satisfied to avoid volume discretization errors [26]. The Chimera technique is yet another alternative for dealing with moving bodies that makes use of independently meshed overlapping zones, typically a grid zone attached to the body and a grid zone for the background domain [27,28]. While the deforming grid approach is required for aeroelastic studies or problems involving moving bodies within fixed multiblock geometries, it can be avoided for the simple heaving and pitching airfoils cases treated in this study. Consequently, a simple rigid body approach is retained with the mesh position $\boldsymbol{x}$ directly derived from the law of motion and the grid velocity $\boldsymbol{s}$ computed using the simple analytical relationship

$$\boldsymbol{s}(t) = \boldsymbol{\Omega}(t)\wedge(\boldsymbol{x}(t) - \boldsymbol{x}_c(t)) + \boldsymbol{t} \quad (9)$$

where $\boldsymbol{\Omega}$ is the rotational velocity vector, $\boldsymbol{x}_c$ the center of rotation and $\boldsymbol{t}$ the translation velocity vector. For the sake of clarity and without loss of generality, the DTS resolution is left aside in this section. Using a second-order BDF for the physical time derivative in Eq. (8) yields the following second-order discretization of the ALE–AC system:

$$\boldsymbol{K}\frac{(\frac{3}{2}\boldsymbol{w}^{n+1}_i - 2\boldsymbol{w}^n_i + \frac{1}{2}\boldsymbol{w}^{n-1}_i)}{\Delta t} + \mathcal{R}^E_i(\boldsymbol{w}^{n+1},\boldsymbol{x}^{n+1},\boldsymbol{s}^{n+1}) = \mathcal{R}^V_i(\boldsymbol{w}^{n+1},\boldsymbol{x}^{n+1}) \quad (10)$$

3. Implicit Time Integration

The fully discrete ALE–AC system (10) can also be expressed as

$$\boldsymbol{K}\frac{(\frac{3}{2}\boldsymbol{w}^{n+1}_i - 2\boldsymbol{w}^n_i + \frac{1}{2}\boldsymbol{w}^{n-1}_i)}{\Delta t} + \mathcal{R}_i(\boldsymbol{w}^{n+1}) = 0 \quad (11)$$

with the full residual $\mathcal{R}$ defined by $\mathcal{R}_i(\boldsymbol{w}^{n+1}) = \mathcal{R}^E_i(\boldsymbol{w}^{n+1}) - \mathcal{R}^V_i(\boldsymbol{w}^{n+1})$, where the dependence on the grid position and velocity has been omitted for the sake of simplicity. The nonlinear system (11) is solved using a DTS approach, that is the new state $\boldsymbol{w}^{n+1}$ is iteratively obtained as the steady solution with respect to the dual time τ of the augmented system:

$$\frac{\boldsymbol{w}^{n,m+1}_i - \boldsymbol{w}^{n,m}_i}{\Delta\tau^{n,m}_i} + \boldsymbol{K}\frac{(\frac{3}{2}\boldsymbol{w}^{n,m}_i - 2\boldsymbol{w}^n_i + \frac{1}{2}\boldsymbol{w}^{n-1}_i)}{\Delta t} + \mathcal{R}_i(\boldsymbol{w}^{n,m}) = 0 \quad (12)$$

where $\boldsymbol{w}^{n,m}$ is the fictitious state at the mth subiteration on τ performed between the nth and $(n+1)$th physical time levels. The initial fictitious state at each physical time level is chosen as $\boldsymbol{w}^{n,0} = \boldsymbol{w}^n$ and the new physical state is defined as $\boldsymbol{w}^{n+1} = \boldsymbol{w}^{n,m_{\max}}$ with $m_{\max}$ the number of subiterations on τ needed to achieve steady-state

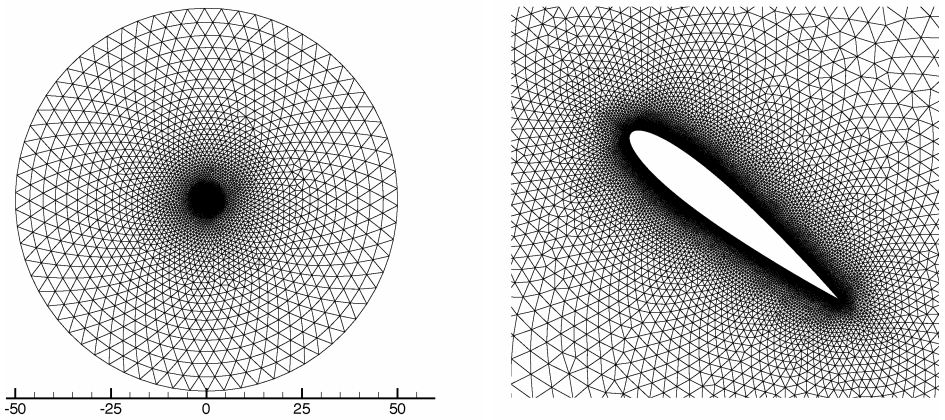

a) b)

Fig. 1 Views of the computational grid: a) global view and b) close-up on the airfoil region.

convergence of Eq. (12). The efficiency of the method is ensured by making use of an implicit dual-time integration:

$$\frac{\Delta \boldsymbol{w}_i^{n,m}}{\Delta \tau_i^{n,m}} = -\mathcal{R}_i(\boldsymbol{w}^{n,m+1}) - \boldsymbol{K}\frac{(\frac{3}{2}\boldsymbol{w}_i^{n,m+1} - 2\boldsymbol{w}_i^{n} + \frac{1}{2}\boldsymbol{w}_i^{n-1})}{\Delta t} = -\mathcal{R}_i^t(\boldsymbol{w}^{n,m+1}) \tag{13}$$

with $\boldsymbol{w}^{n,m+1} = \boldsymbol{w}^{n,m} + \Delta \boldsymbol{w}^{n,m}$. Since the solution accuracy (on t and x) does not depend on the dual-time increment $\Delta \boldsymbol{w}^{n,m}$ which goes to zero at steady state on τ, the full residual $\mathcal{R}_i^t(\boldsymbol{w}^{n,m+1})$ can be expanded as

$$\mathcal{R}_i^{\,t}(\boldsymbol{w}^{n,m+1}) = \mathcal{R}_i^t(\boldsymbol{w}^{n,m}) + \boldsymbol{K}\frac{3}{2}\frac{\Delta \boldsymbol{w}_i^{n,m}}{\Delta t} + \frac{1}{|\Omega_i|}\sum_k (\Delta \mathcal{H}_{i,k}^{(i)})^{n,m}|\Gamma_{i,k}| \tag{14}$$

where $(\Delta \mathcal{H}_{i,k}^{(i)})^{n,m} = \mathcal{H}^{(i)n,m+1} - \mathcal{H}^{(i)n,m}$ and $\mathcal{H}^{(i)} = \mathcal{H}^{E(i)} - \mathcal{H}^{V(i)}$ denotes the numerical flux formula retained in the implicit stage. Since the implicit stage vanishes at steady state this numerical flux formula does not impact the overall accuracy and its design is solely guided by stability and efficiency requirements. Following [24,29,30] the inviscid numerical flux $\mathcal{H}^{E(i)}$ appearing in the implicit stage is simply computed using the first-order Rusanov numerical flux:

$$\mathcal{H}_{i,k}^{E(i)} = \frac{1}{2}(\boldsymbol{F}_i^E \cdot \boldsymbol{n}_{i,k} + \boldsymbol{F}_{o(i,k)}^E \cdot \boldsymbol{n}_{i,k}) + \frac{1}{2}\rho(\boldsymbol{J}_\perp^E)_{i,k}(\boldsymbol{w}_i - \boldsymbol{w}_{o(i,k)}) \tag{15}$$

where $\rho(\boldsymbol{J}_\perp^E)_{i,k}$ is the spectral radius of the inviscid Jacobian matrix $\boldsymbol{J}_\perp^E$ computed at the center of face $\Gamma_{i,k}$. The implicit numerical viscous flux takes the following simplified form:

$$\mathcal{H}_{i,k}^{V(i)} = \frac{\rho(\boldsymbol{J}_\perp^V)_{i,k}}{\|\boldsymbol{r}_{i,k}\| + \|\boldsymbol{r}_{o(i,k)}\|}(\boldsymbol{w}_{o(i,k)} - \boldsymbol{w}_i) = \widetilde{\rho(\boldsymbol{J}_\perp^V)}_{i,k}(\boldsymbol{w}_{o(i,k)} - \boldsymbol{w}_i) \tag{16}$$

where $\rho(\boldsymbol{J}_\perp^V)_{i,k}$ is the spectral radius of the viscous Jacobian matrix. More details on the derivation of the implicit viscous flux can be found in [15]. Inserting the expressions Eqs. (15) and (16) of the implicit numerical fluxes into the expansion of the residual Eq. (14) and rearranging Eq. (13) yields the following implicit solution for the ALE–AC system (10):

$$\boldsymbol{D}_i^{n,m}\Delta \boldsymbol{w}_i^{n,m} + \frac{1}{2|\Omega_i|}\sum_k (\Delta \boldsymbol{F}_{o(i,k)}^E)^{n,m} \cdot \boldsymbol{n}_{i,k}|\Gamma_{i,k}| - \sum_k C_{i,k}^{n,m}\Delta \boldsymbol{w}_{o(i,k)}^{n,m} = -\mathcal{R}_i^t(\boldsymbol{w}^{n,m}) \tag{17}$$

The coefficients $\boldsymbol{D}_i^{n,m}$, $C_{i,k}^{n,m}$ are defined by

$$\boldsymbol{D}_i^{n,m} = \left(\frac{\boldsymbol{I}}{\Delta \tau_i^{n,m}} + \frac{3}{2}\frac{\boldsymbol{K}}{\Delta t} + \sum_k C_{i,k}^{n,m}\boldsymbol{I}\right), \quad C_{i,k}^{n,m} = \frac{1}{|\Omega_i|}\left(\frac{1}{2}\rho(\boldsymbol{J}_\perp^E) + \widetilde{\rho(\boldsymbol{J}_\perp^V)}\right)_{i,k}^{n,m}|\Gamma_{i,k}| \tag{18}$$

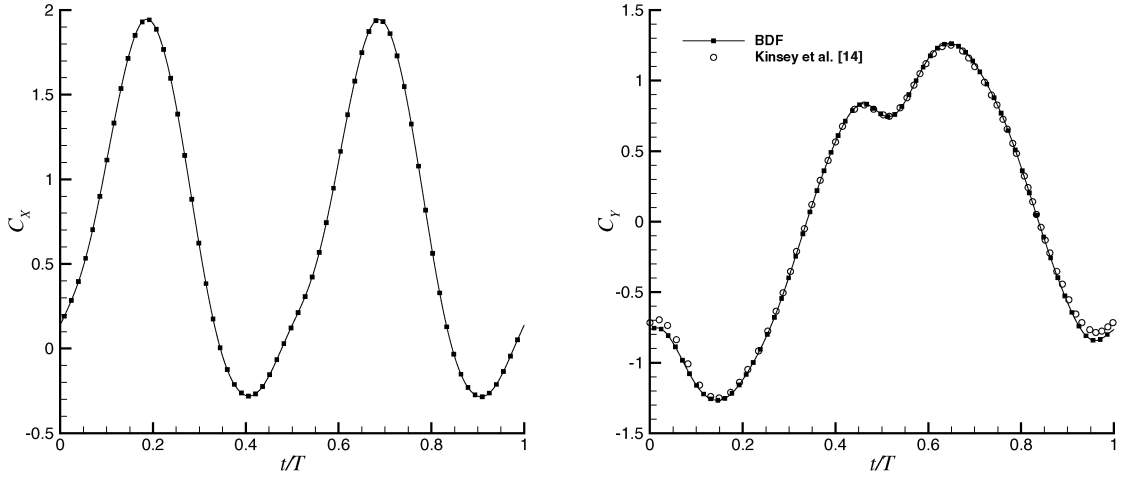

a) b)

Fig. 2 PH test case: a) C_X evolution computed using the present BDF method and b) C_Y evolution computed in [14] and using the present BDF method.

with $\boldsymbol{I}$ the identity matrix; note the implicit stage is in fact matrix-free with a scalar diagonal coefficient D for $\Delta p_i^{n,m}$ deprived from the $3/(2\Delta t)$ contribution in the mass conservation equation and including this term in the momentum conservation equations which involve $\Delta u_i^{n,m}$ and $\Delta v_i^{n,m}$. Equation (17) can be solved at a very low cost per iteration using a simple point-Jacobi (PJ) relaxation method. Denoting l the iteration counter associated with this method when Eq. (17) is iteratively solved to obtain $\boldsymbol{w}^{n,m+1}$ from the known $\boldsymbol{w}^{n,m}$ and introducing $\Delta\phi^{(l)} = \phi^{(l)} - \phi^{n,m}$, the PJ–BDF–ALE–AC procedure reads

$$\Delta \boldsymbol{w}_i^{(0)} = 0 \qquad \begin{cases} l = 0, l_{\max} - 1 \\ \Delta \boldsymbol{w}_i^{(l+1)} = (\boldsymbol{D}_i^{n,m})^{-1}\left(-\mathcal{R}_i^t(\boldsymbol{w}^{n,m}, \boldsymbol{x}^{n+1}, \boldsymbol{s}^{n+1}) - \frac{1}{2|\Omega_i|}\sum_k (\Delta \boldsymbol{F}^E_{o(i,k)})^{(l)} \cdot \boldsymbol{n}_{i,k}|\Gamma_{i,k}| + \sum_k C^{n,m}_{i,k}\Delta \boldsymbol{w}^{(l)}_{o(i,k)}\right) \end{cases} \tag{19}$$

$$\boldsymbol{w}_i^{n,m+1} = \boldsymbol{w}_i^{n,m} + \Delta \boldsymbol{w}_i^{(l_{\max})}$$

C. Solver Validation

The solver presented in the previous section is validated by computing incompressible unsteady laminar flows over pitching and heaving airfoils which were recently studied by Kinsey and Dumas [14]. The airfoil flow computations presented in [14] were performed using a conventional pressure-based solver implemented in a commercial solver on very fine grids and with a very small time step to ensure time and grid convergence and allow a fine analysis of the flowfield. These computations will therefore be retained as first reference data and the ability of the proposed PJ–BDF–ALE–AC to provide similar results will be established in the present section.

1. Test-Cases Description

The geometry under study is a NACA0015 airfoil submitted to a pitching motion and/or a heaving motion. These prescribed motions are defined by the following laws of evolution for the pitching angle $\theta(t)$, around an axis located at one third of the airfoil chord, and the vertical position $y(t)$:

$$\begin{cases} \theta(t) = \theta_0 \sin(\omega t) \\ y(t) = H_0 \sin\left(\omega t + \frac{\pi}{2}\right) \end{cases} \tag{20}$$

where θ_0 and H_0 are, respectively, the pitching and heaving amplitudes, ω is the angular velocity. The reduced frequency f^* is defined as $f^* = fc/U_\infty$, where U_∞ is the freestream velocity. The first test case (PH) combines pitching and heaving motion with $\theta_0 = 60°$, $H_0 = 1$ and $f^* = 0.18$. The second test case (PP) corresponds to a pure pitching motion with $\theta_0 = 23°$, $H_0 = 0$ and $f^* = 0.12$. In both cases, the Reynolds number based on the freestream conditions and the airfoil chord is equal to $Re = 1100$ hence the flow is assumed laminar.

2. Numerical Parameters

The computational mesh displayed in Fig. 1 was generated so as to be similar to the grid used in [14] since both the proposed PJ–BDF–ALE–AC solver and the commercial solver used by Kinsey and Dumas are second-order methods on unstructured triangular grids. This mesh counts 32,000 cells, with 360 points set on the airfoil and a near body resolution tailored to satisfy the criterion $y_p^2(U_\infty/\nu_\infty\Delta) \sim 1$, where y_p is the distance from the wall to the first adjacent cell centroid and Δ is the minimal edge length on the airfoil. The enforcement of this criterion combines a low-cell-Reynolds number and a moderate cell aspect ratio near the airfoil surface to ensure solution accuracy. The AC parameter β is constant and equal to five; this value was retained as offering a good tradeoff between accuracy and efficiency after a careful assessment of the flow solver on several incompressible reference flows (this study is not reproduced for the sake of conciseness and because the focus of the present work is on the TSM approach applied to the AC solver, not on the AC solver itself).

For each case, 520 physical time steps per period or cycle are used corresponding to a fixed nondimensional value of $\Delta t \approx 1.06^{-2}$ and $\Delta t \approx 1.16^{-2}$ for the PH an PP test cases, respectively. The local DTS is computed as $\Delta\tau_i^{n,m} = \mathrm{CFL}\max(h_i/(\rho^E)_i^{n,m}, h_i^2/(2\rho^V)_i^{n,m})$ with h_i a characteristic length of the cell Ω_i, ρ^E and ρ^V the spectral radii of the inviscid and viscous Jacobian matrices and CFL the multiplication factor of the characteristic time step chosen as large as possible, $\mathrm{CFL} = 10^6$, to ensure fast convergence to the dual steady state through the use of very large values for $\Delta\tau_i^{n,m}$. At each physical time step, 100 dual-time iterations are performed with 16 iterations of the PJ method to solve Eq. (19). The residual drops by three to four orders of magnitude for all the time instants of a cycle; it has been checked that this criterion is sufficient to obtain converged results (global aerodynamic coefficients, wall distribution, fields).

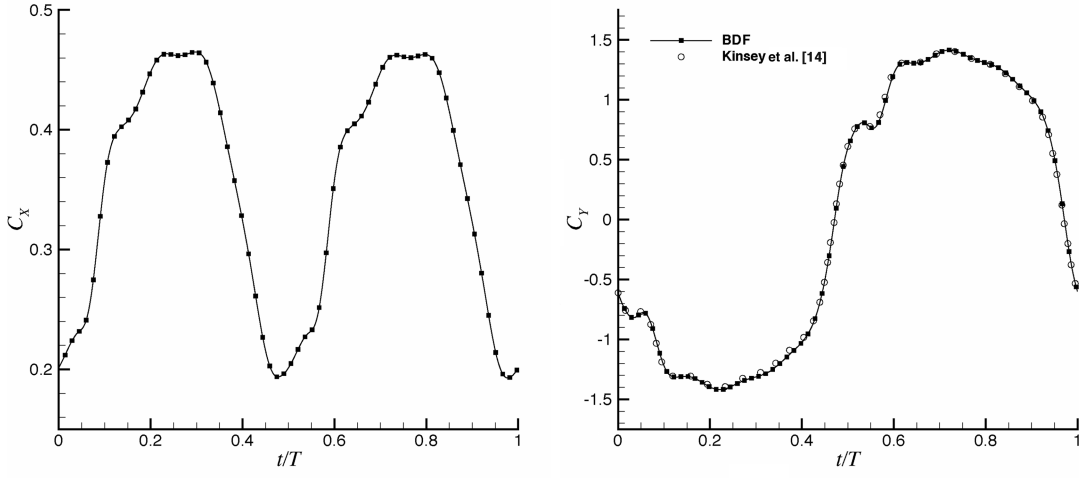

Fig. 3 PP test case: a) C_X evolution computed using the present BDF method and b) C_Y evolution computed in [14] and using the present BDF method.

The computation is started with a uniform pressure and velocity flowfield; six (respectively four) cycles must be computed for PH (respectively PP) before flow periodicity is fully achieved. A variation of the mean aerodynamic coefficient inferior to 0.2% between two consecutive cycles is the criterion typically used to ensure a fully periodic flow is obtained. All the PJ–BDF–ALE–AC results displayed hereafter correspond to the seventh cycle for PH and fifth cycle for PP and will be labeled BDF from now on.

3. Results

The comparison with the reference results [14] is performed on the force coefficients, more precisely on the C_Y coefficient which is the only one made available by Kinsey and Dumas. The C_X coefficient is also presented for future comparison with the TSM approach. Figure 2 presents the computed C_X and C_Y coefficients over the normalized time period for the PH test case; note only one out of eight physical time steps are plotted for the present BDF computations. Similar results obtained for the PP test case are plotted in Fig. 3. The agreement between [14] and the present BDF results is globally very good. A slight difference on the C_Y prediction can be observed in Fig. 2 for the PH problem. Further grid and time refinement did not modify the present BDF results which will consequently be retained as reference data, against which the TSM approach developed in the next section will be compared, both in terms of accuracy and efficiency.

III. AC and TSM

The present section explains how the time spectral method, essentially used up to now in the context of compressible flows for structured grid computations, can be combined with the unstructured AC solver described in the previous section. The straightforward application of the TSM for the ALE–AC system is first explained; next, the method of resolution of the AC–ALE TSM discretization is described and the necessary modifications to perform on the implicit treatment are detailed.

A. TSM Discretization of ALE–AC System

Taking advantage of the time periodicity of $\boldsymbol{w}$, the solution vector can be decomposed into a Fourier series:

$$\boldsymbol{w} = \sum_{k=-\infty}^{+\infty} \hat{\boldsymbol{w}}_k(x) e^{\underline{i} k\omega t} \tag{21}$$

where ω is the pulsation of the periodic phenomenon related to the period T by $\omega = 2\pi/T$. The complex number $\underline{i}$ is underlined to avoid confusion with the cell index i. In practice, the solution is represented with a finite number of harmonics N:

$$\boldsymbol{w} = \sum_{k=-N}^{N} \hat{\boldsymbol{w}}_k(x) e^{\underline{i} k\omega t} \tag{22}$$

The Nyquist–Shannon theorem [31] states that the kth Fourier coefficient $\hat{\boldsymbol{w}}_k$ with $-N \le k \le N$ can be accurately computed with $2N+1$ time instances evenly distributed over the time period:

$$\hat{\boldsymbol{w}}_k(x) = \frac{1}{2N+1} \sum_{n=0}^{2N} \boldsymbol{w}_n e^{-\underline{i} k\omega n \Delta t} \tag{23}$$

with $\boldsymbol{w}_n \equiv \boldsymbol{w}(t_n = n\Delta t)$ and $\Delta t = T/(2N+1)$. The main idea of the TSM [4] is then to look for these solutions $\boldsymbol{w}_n$ in order to retrieve the solution at any time t in the period using Eq. (22). The space-discretized ALE–AC system at time instance t_n reads

$$\boldsymbol{K} \frac{\partial \boldsymbol{w}_n}{\partial t} + \mathcal{R}(\boldsymbol{w}_n, \boldsymbol{x}_n, \boldsymbol{s}_n) = 0 \tag{24}$$

where $\boldsymbol{w} = \{\boldsymbol{w}_i\}$ is the set of solution values in all the grid cells and $\mathcal{R} = \{\mathcal{R}_i\}$ is the set of residual values computed in all the grid cells, which depends nonlinearly on $\boldsymbol{w}$. From now on, $\boldsymbol{w}_{i,n}$ will denote the solution at the grid point i and the nth time instance t_n in the period.

Using the Fourier decomposition Eq. (22) of $\boldsymbol{w}_n$ into Eq. (24) leads to $2N+1$ equations (one for each wave number) in the frequency domain:

$$\boldsymbol{K} \sum_{k=-N}^{N} \underline{i} k\omega \hat{\boldsymbol{w}}_k e^{\underline{i} k\omega n \Delta t} + \hat{\mathcal{R}}(\hat{\boldsymbol{w}}_k, \hat{\boldsymbol{x}}_k, \hat{\boldsymbol{s}}_k) = 0 \tag{25}$$

The operator $\hat{\mathcal{R}}$ could be directly computed from $\hat{\boldsymbol{w}}_k$ but, because of its nonlinearity, this would involve complex series of convolution becoming massively time consuming [3]. Using Eq. (23) allows to cast system (25) back into the time domain and to retrieve the original residual vector $\mathcal{R}$ because of the bijective property of the Fourier transform

$$\boldsymbol{K} D_t(\boldsymbol{w}_n) + \mathcal{R}(\boldsymbol{w}_n, \boldsymbol{x}_n, \boldsymbol{s}_n) = 0 \tag{26}$$

where $D_t(\boldsymbol{w}_n)$ is the spectral derivative with respect to time that couples the wave numbers. The spectral time operator expressed in the time domain becomes

$$D_t(\boldsymbol{w}_n) = \sum_{p=-N}^{N} d_p \boldsymbol{w}_{n+p} \tag{27}$$

In Eq. (27) the subscript $n+p$ must be understood as expressed modulo $2N+1$ to get the corresponding positive subscript. For instance $w_{-N} = w_{N+1}$. The d_p coefficients are given by

$$d_p = \begin{cases} \frac{\pi}{T}(-1)^{(p+1)} \csc\left(\frac{\pi p}{2N+1}\right) & \text{if } p \neq 0 \\ 0 & \text{if } p = 0 \end{cases} \tag{28}$$

Since the spectral time derivative depends on the whole set of solutions w_{n+p} with p ranging from $-N$ to N, system (26) must be written for each time instance in the period:

$$\boldsymbol{K} D_t(\boldsymbol{w}_n) + \mathcal{R}(\boldsymbol{w}_n, \boldsymbol{x}_n, \boldsymbol{s}_n) = 0, \qquad 0 \le n < 2N+1 \tag{29}$$

B. Resolution of TSM–ALE–AC System

The nonlinear system of Eq. (29) is iteratively solved through a dual-time-marching strategy, that is looking for the steady state with respect to τ of the following system:

$$\frac{\partial \boldsymbol{w}_n}{\partial \tau} = -\mathcal{R}_n^t(\boldsymbol{w}, \boldsymbol{x}_n, \boldsymbol{s}_n), \qquad 0 \le n < 2N+1 \tag{30}$$

where the total residual is defined as $\mathcal{R}_n^t(\boldsymbol{w}) = KD_t(\boldsymbol{w}_n) + \mathcal{R}(\boldsymbol{w}_n, \boldsymbol{x}_n, \boldsymbol{s}_n)$ for the TSM approach. The $2N+1$ steady values $\boldsymbol{w}_n$ are coupled through the spectral approximation $D_t(\boldsymbol{w}_n)$ of the physical time derivative. Let us denote $\boldsymbol{w}_n^m$ the intermediate value of $\boldsymbol{w}_n$ at the mth iteration of the dual-time evolution to a steady state. Using a simple first-order Euler explicit discretization for the dual-time derivative, the steady state is reached by iteratively solving

$$\frac{\Delta \boldsymbol{w}_n^m}{\Delta \tau_{i,n}^m} = -\mathcal{R}_n^t(\boldsymbol{w}^m, \boldsymbol{x}_n, \boldsymbol{s}_n), \qquad 0 \le n < 2N+1 \tag{31}$$

where $\Delta \boldsymbol{w}_n^m = \boldsymbol{w}_n^{m+1} - \boldsymbol{w}_n^m$ and $\Delta \tau_{i,n}^m$ is the local (dual) time step in cell i of the grid associated with the time instance t_n within the period. Note that, in the present study, the $2N+1$ grid positions and velocities are a priori known from the prescribed grid motion. In particular, the velocity $\boldsymbol{s}_n$ is calculated with Eq. (9) at time t_n Adapting to the present AC system the stability analysis conducted in [5] for TSM compressible flow computations using an explicit formulation similar to Eq. (31) leads to the following CFL-like stability condition for the choice of $\Delta \tau_{i,n}^m$:

$$\Delta \tau_{i,n}^m = \mathrm{CFL} \frac{h_i}{\|\lambda\|_{i,n}^m + N\omega h_i} \tag{32}$$

with h_i a characteristic length of the cell i in the computational grid, $\|\lambda\|_{i,n}^m$ the spectral radius of the Jacobian matrix associated with the inviscid AC system at time instance t_n and $\mathrm{CFL} \le 1$. Looking for the

solution of a steady incompressible flow, the matrix K would be equal to zero and the preceding condition would not include the $N\omega h_i$ contribution. When the explicit TSM scheme is applied to obtain the solution of a periodic incompressible flow with either a high frequency ($\omega \gg 1$) and/or a high number N of harmonics, condition (32) can become particularly restrictive. Using an Euler implicit dual-time integration for integrating Eq. (30) in each grid cell i at each time instance t_n allows the use of large DTSs, hence fast convergence to a steady state independently of ω or N, but the following implicit nonlinear TSM–ALE–AC problem must be solved:

$$\frac{\Delta \boldsymbol{w}_{i,n}^m}{\Delta \tau_{i,n}^m} = -\mathcal{R}_{i,n}^t(\boldsymbol{w}^{m+1}, \boldsymbol{x}_n, \boldsymbol{s}_n), \qquad 0 \le n < 2N+1 \tag{33}$$

when going from the BDF to the TSM system: while the BDF formula strengthens the diagonal dominance of the linear system associated with the implicit stage, the TSM formula introduces only off-diagonal terms which lead to a loss of diagonal dominance. This issue was pointed out by Su and Yuan in [8] and the problem was then fixed by using the GMRES solver of Saad and Schultz [32] to solve the implicit TSM system. Woodgate and Badcock [7] also highlight the performance reduction of their Krylov linear solver due to the loss of diagonal dominance for the matrix of the implicit system. In the present work, a simple fix is adopted: the LHS coefficient of $\Delta \boldsymbol{w}_{i,n}^m$ in system (35) is modified to include the contribution $\boldsymbol{K} \sum_{p=-N}^{p=N} |d_p|$, which is sufficient to ensure the diagonal dominance of the implicit stage with only a limited impact on its efficiency. System (35) is then iteratively solved using a simple PJ relaxation technique, yielding the following PJ–TSM–ALE–AC system:

$$\Delta \boldsymbol{w}_{i,n}^{(0)} = 0 \qquad \begin{cases} l = 0, l_{\max} - 1 \\ \Delta \boldsymbol{w}_{i,n}^{(l+1)} = (\boldsymbol{D}_{i,n}^m)^{-1} \\ \left(-\mathcal{R}_{i,n}^t(\boldsymbol{w}^m) - \frac{1}{2|\Omega_{i,n}|} \sum_k (\Delta \boldsymbol{F}_{o(i,k),n}^E)^{(l)} \cdot \boldsymbol{n}_{(i,k),n} |\Gamma_{(i,k),n}| + \sum_k C_{(i,k),n}^m \Delta \boldsymbol{w}_{(o(i,k)),n}^{(l)} - \boldsymbol{K} \sum_{p=-N}^N d_p \Delta \boldsymbol{w}_{i,n+p}^{(l)} \right) \end{cases} \tag{37}$$

$$\boldsymbol{w}_{i,n}^{m+1} = \boldsymbol{w}_{i,n}^m + \Delta \boldsymbol{w}_{i,n}^{(l_{\max})}$$

C. Implicit TSM: PJ–TSM–ALE–AC System

The full TSM residual is defined by $\mathcal{R}^t(\boldsymbol{w}) = \boldsymbol{K} D_t(\boldsymbol{w}) + \mathcal{R}(\boldsymbol{w})$ with the spectral difference operator Dt linear and the spatial discretization operator $\mathcal{R}$ formally unchanged with respect to the BDF approach. Following a line of work similar to that described for the BDF approach, the TSM residual at dual-time level $m+1$ can be approximated as follows:

$$\mathcal{R}_{i,n}^t(\boldsymbol{w}^{m+1}) = \mathcal{R}_{i,n}^t(\boldsymbol{w}^m) + \boldsymbol{K} D_t(\Delta \boldsymbol{w}_{i,n}^m) + \frac{1}{|\Omega_i|} \sum_k \left(\Delta \mathcal{H}_{(i,k),n}^{(i)} \right)^m |\Gamma_{i,k}| \tag{34}$$

where the flux increment balance $\Delta \mathcal{H}^{(i)}$ is computed using Eqs. (15) and (16) previously introduced when deriving the BDF implicit stage but now applied with the variable increment $\Delta \boldsymbol{w}_{i,n}^m$ instead of $\Delta \boldsymbol{w}_i^{n,m}$. Expanding this flux increment balance and the spectral approximation of the physical time derivative with Eqs. (27) and (28) leads to the following implicit relationship, where the terms depending on $\Delta \boldsymbol{w}_{i,n}^m$ have been gathered in the left-hand side (LHS):

$$\left(\frac{1}{\Delta \tau_{i,n}^m} + \sum_k C_{(i,k),n}^m \right) \Delta \boldsymbol{w}_{i,n}^m = -\mathcal{R}_{i,n}^t(\boldsymbol{w}^m) - \frac{1}{2|\Omega_{i,n}|} \sum_k (\Delta \boldsymbol{F}_{o(i,k),n}^E)^m \cdot \boldsymbol{n}_{(i,k),n} |\Gamma_{(i,k),n}| + \sum_k C_{(i,k),n}^m \Delta \boldsymbol{w}_{(o(i,k)),n}^m - \boldsymbol{K} \sum_{p=-N}^N d_p \Delta \boldsymbol{w}_{i,n+p}^m \tag{35}$$

with the scalar coefficients $C_{(i,k),n}^m$ defined by

$$C_{(i,k)n}^m = \frac{1}{|\Omega_{i,n}|} \left(\frac{1}{2} \rho(\boldsymbol{J}_\perp^E) + \widetilde{\rho(\boldsymbol{J}_\perp^V)} \right)_{(i,k),n}^m |\Gamma_{(i,k),n}| \tag{36}$$

and $d_0 = 0$ in the spectral time derivative so that there is no contribution of this term to the preceding LHS. Following the strategy adopted to solve the BDF–ALE–AC system, a PJ strategy could be applied to obtain an iterative solution of the preceding TSM–ALE–AC system. However, a significant difference arises with the modified diagonal coefficient $\boldsymbol{D}_{i,n}^m = \frac{1}{\Delta \tau_{i,n}^m} + \sum_k C_{(i,k),n}^m + \boldsymbol{K} \sum_{p=-N}^N |d_p|$.

IV. Assessment of TSM Against BDF

The preceding PJ–TSM–ALE–AC method is now applied to the computation of the test problems PH and PP and its results are compared with those obtained using the PJ–BDF–ALE–AC approach. To the best of our knowledge, the only previous application of TSM to the AC system for incompressible laminar periodic flow has been performed by Jameson [13], but with a limited success since stability concerns were encountered for high frequency and/or large number of harmonics. In the present study, the convergence of TSM to a steady state will be first analyzed when the number of modes N is varied for accuracy purpose. The reference BDF strategy and the newly developed TSM approach will then be discussed in terms of accuracy: in particular, the number of modes needed to achieve a sufficient level of accuracy will be investigated for test problems PH and PP. The potential efficiency gain offered by TSM with respect to BDF will be finally assessed.

A. Convergence of TSM Approach

The convergence of Eq. (37) to a steady state is monitored by plotting the pressure residual defined as the root mean square (RMS) of the residual operator $\mathcal{R}^t(\boldsymbol{w})$ first component, computed in all the grid cells and averaged by the number of time instances over the period:

$$\mathrm{res}_{\mathrm{av}}^m = \frac{1}{2N+1} \sum_{n=0}^{2N} \sqrt{\frac{1}{N_{\mathrm{cell}}} \sum_{i=1}^{N_{\mathrm{cell}}} \frac{\Delta p_{i,n}^{m^2}}{\Delta \tau_{i,n}^{m^2}}}$$

This quantity is normalized by its value at the first iteration to facilitate the comparison between calculations performed with different values for the number of harmonics N. All the computations make use of $l_{\max} = 16$ for the implicit PJ solver and $\mathrm{CFL} = 10^6$ for computing the DTS $\Delta \tau_{i,n}^m$ with Eq. (32). The AC parameter β is the same as in the previous BDF calculations ($\beta = 5$).

The convergence histories displayed in Fig. 4 demonstrate the convergence rate of the TSM solver to a steady state depends only weakly on the number of modes N: for test case PH, less than 4000

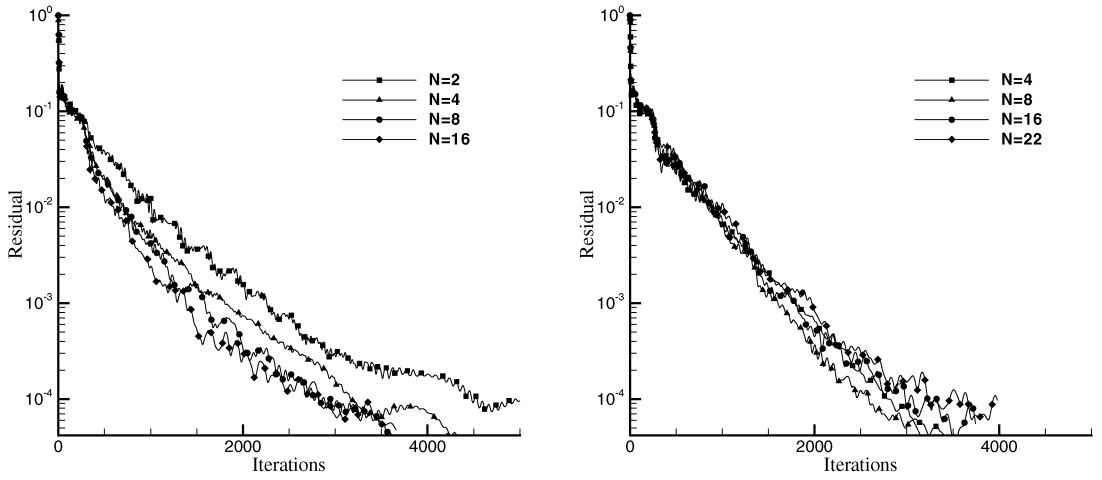

a) b)

Fig. 4 Convergence history for the PJ–TSM–ALE–AC method: a) PH test problem with increasing number of harmonics (N ranging from 2 to 16) and b) PP test problem with increasing number of harmonics (N ranging from 4 to 22).

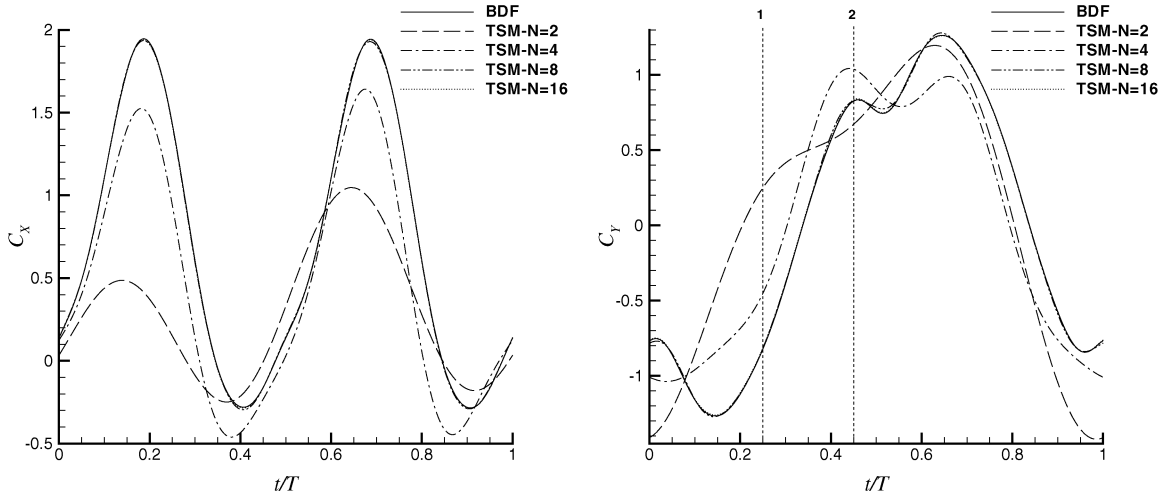

a) b)

Fig. 5 PH test case. Comparison of a) C_X and b) C_Y coefficients computed using BDF and TSM with an increasing number of harmonics.

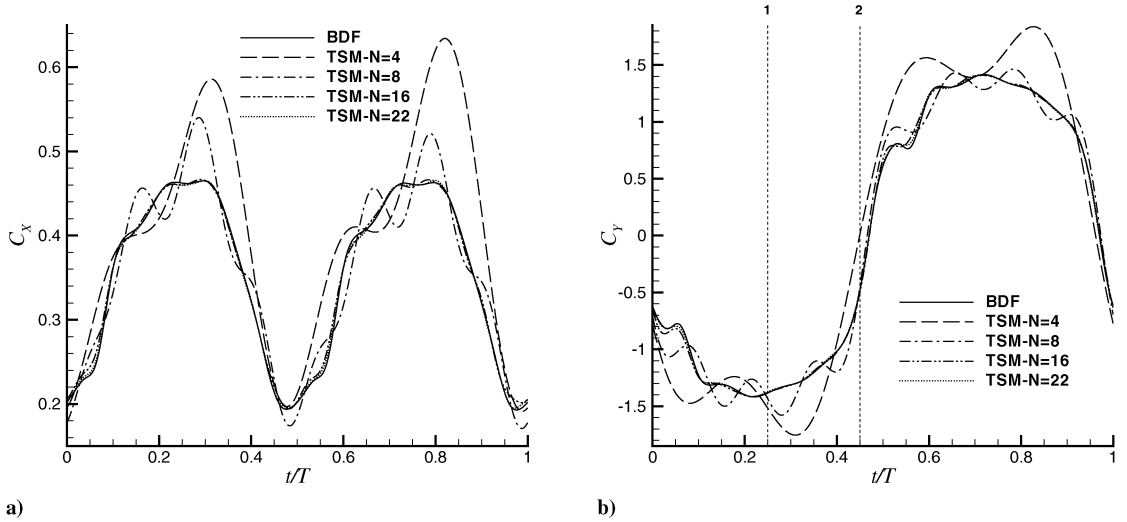

a) b)

Fig. 6 PP test case. Comparison of a) C_X and b) C_Y coefficients computed using BDF and TSM with an increasing number of harmonics.

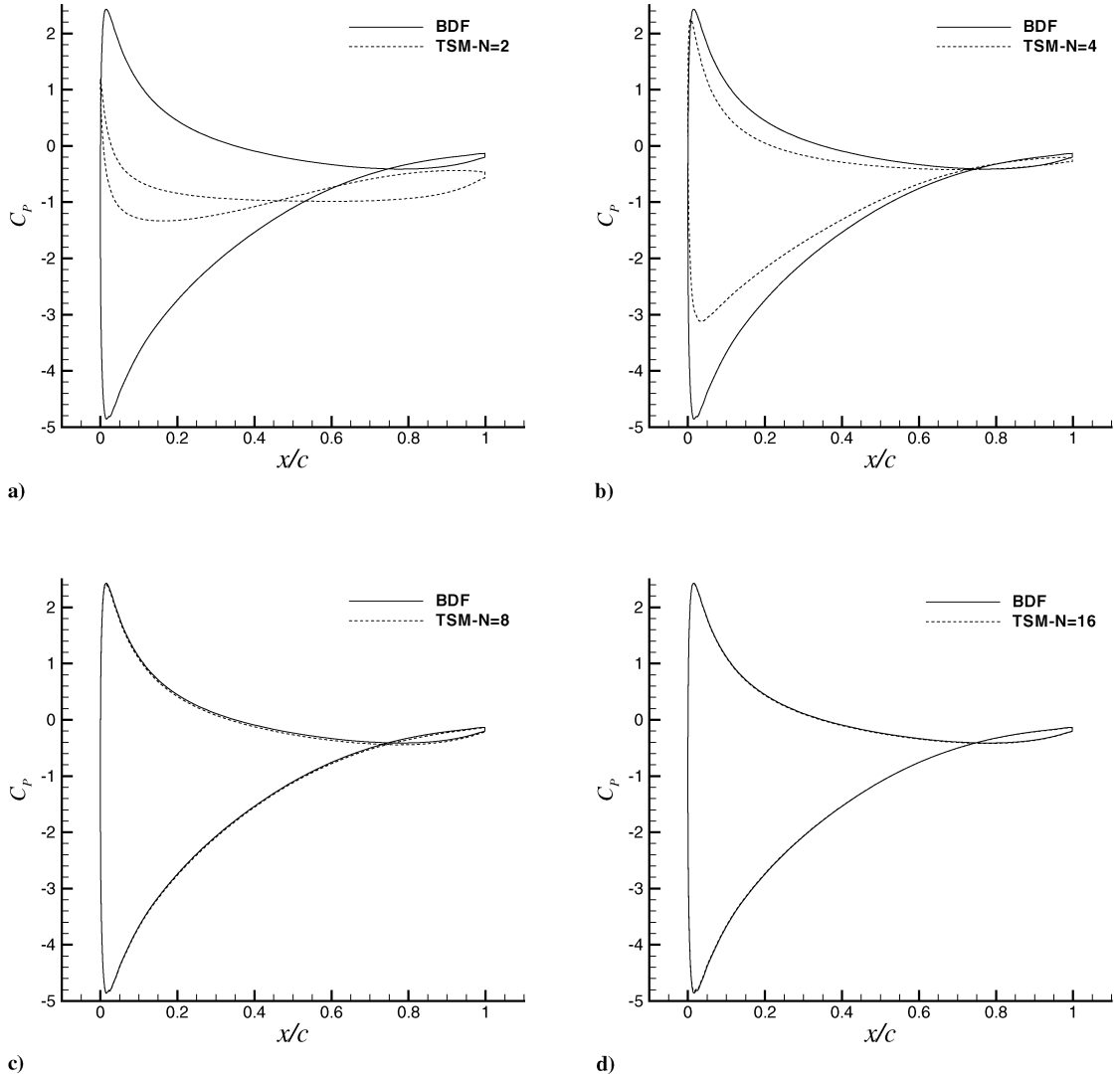

Fig. 7 Flow problem PH. Reconstructed TSM(N) wall pressure coefficient at time $t/T = 0.25$ for an increasing number N of harmonics. Comparison with the reference BDF distribution.

iterations are needed to achieve a residual decrease by four orders of magnitude while a bit less than 3000 iterations are sufficient for test case PP, whatever the value of N. The cost of an iteration depends of course on the value of N but this point will be discussed at the end of the section after analyzing the accuracy of the TSM solutions.

B. Accuracy of TSM Solutions

The accuracy of the TSM solutions will be first assessed in a qualitative way by comparing the steady solutions of the PJ–TSM–ALE–AC system obtained for an increasing number of harmonics with the previously computed BDF solution. This comparison will be performed on the evolution of the global force coefficients C_X, C_Y over a cycle both for the PH and PP test problems. Next the computed wall pressure distribution over the airfoil and pressure contours at selected instants within the period will also be compared. A more quantitative error analysis between TSM and BDF will be eventually proposed and conclusions regarding the potential efficiency gain offered by TSM with respect to BDF will be drawn.

1. Global Aerodynamic Coefficients

Figures 5 and 6 display the C_X and C_Y coefficients computed using the TSM approach with an increasing number of harmonics for the PH and PP flow problems, respectively. These evolutions over a period are plotted along the previously computed BDF results, whose accuracy was checked with respect to [14]. Let us recall the BDF computations use 520 physical time steps per period and require about four (respectively six) cycles before reaching a periodic solution for the PH (respectively PP) flow problem. The TSM evolutions are reconstructed from the computed $\boldsymbol{w}_n$ fields for any time in the period using the truncated Fourier series representation of the flow solution. For the PH test problem, the computed evolution using TSM with $N = 2$ and $N = 4$ significantly differs from the reference result; very small differences between the BDF and TSM evolution remain with $N = 8$ but both evolutions appear superimposed with $N = 16$. For the PP test problem, the computed evolution of C_X and C_Y using TSM with $N = 4$ and $N = 8$ display significant differences with the reference result; with $N = 16$ there are still some very small discrepancies while with $N = 22$ the BDF and TSM results appear as superimposed.

2. Wall Pressure Distributions and Pressure Fields

Two moments within the period are retained for a closer comparison of the computed flowfields: $t/T = 0.25$ and $t/T = 0.45$. For each of these moments, the wall pressure coefficient distribution obtained by using BDF and TSM(N) is plotted, respectively, in Fig. 7 and 8 for test problem PH. Let us recall these pressure distributions are reconstructed at each grid point i from the computed $\boldsymbol{w}_{i,n}$ values, applying Eqs. (22) and (23) in each grid cell. For the PH computation, the already very good agreement between BDF and TSM(8) and the almost perfect match between BDF and TSM(16) wall distributions are clearly visible. For test problem PP, the wall pressure coefficient distribution obtained by using BDF and TSM(N) is plotted,

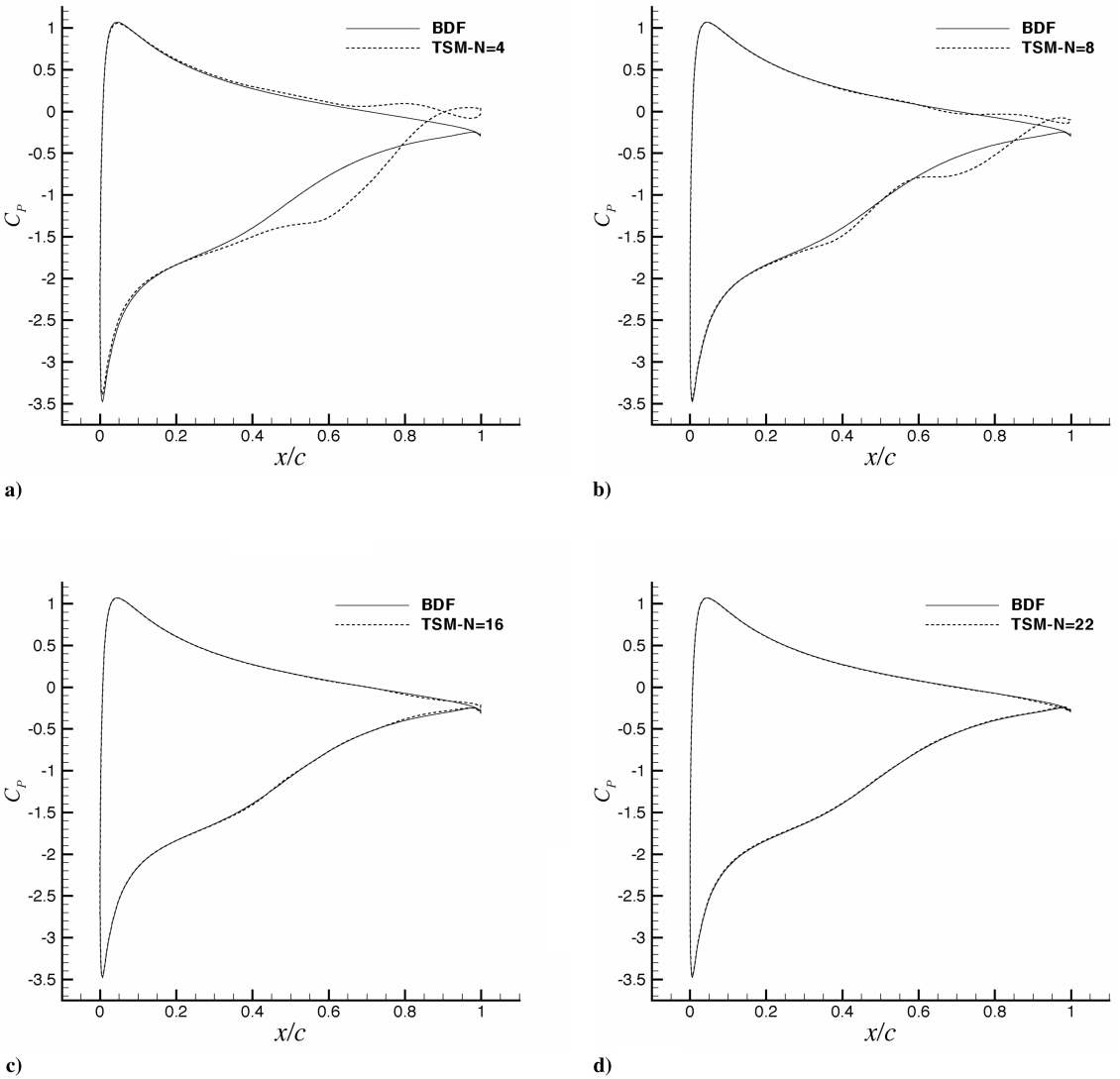

Fig. 8 Flow problem PH. Reconstructed TSM(N) wall pressure coefficient at time $t/T = 0.45$ for an increasing number N of harmonics. Comparison with the reference BDF distribution.

respectively, in Figs. 9 and 10. The match is already very good with $N = 16$ and almost perfect when $N = 22$. The similarity involving BDF and TSM(8) and TSM(16) wall distributions is confirmed on the pressure contours displayed in Fig. 11, and the similarity involving BDF and TSM(N) is confirmed on the pressure contours displayed in Fig. 12.

3. Quantitative Error Analysis

The RMS error on the C_X force coefficient is defined as:

$$\epsilon_{\mathrm{RMS}}(C_X) = \sqrt{\frac{1}{N_{\Delta t}} \sum_{k=1}^{N_{\Delta t}} \left(\frac{(C_X)_{\mathrm{TSM}(N)}(t_k) - (C_X)_{\mathrm{BDF}}(t_k)}{(\Delta C_X)_{\mathrm{BDF}}} \right)^2}$$

where the values of the C_X coefficients at times t_k in the flow cycle and the amplitude ΔC_X of the C_X variation are readily available for the BDF computation while the values of C_X corresponding to the TSM computation are obtained by reconstruction of the flow solution using a truncation Fourier series with N harmonics. The RMS error on the C_Y force coefficient is similarly defined. These errors are plotted as a function of N in Fig. 13 to conclude on the best choice of N: the number of harmonics must indeed be taken large enough to ensure the computed TSM solution is sufficiently accurate with respect to the usual BDF solution but not unnecessarily large since the gain expected from the TSM approach with respect to the BDF strategy is a cost reduction rather than an increased accuracy. Consistently with the previous graphical comparisons between BDF and TSM solutions, the error levels achieved on test problem PH for a given number of harmonics are much lower than the errors levels obtained on test problem PP. For test case PH, the RMS error on C_X and C_Y drops below the 1% level for $N = 8$ while $N = 16$ is needed to fulfill this same criterion for test case PP.

C. Efficiency of TSM Approach

The global computational cost of the usual BDF approach can be expressed as:

$$\mathcal{C}_{\mathrm{BDF}} = N_{\Delta t} \times N_{\mathrm{cycles}} \times m_{\mathrm{max}}^{\mathrm{BDF}} \times l_{\mathrm{max}} \times N_{\mathrm{cells}} \times c_u^{\mathrm{BDF}}$$

where $N_{\Delta t}$ is the number of physical time steps used to describe a flow period or cycle, N_{cycles} is the number of cycles to be computed before a periodic solution is actually reached, $m_{\mathrm{max}}^{\mathrm{BDF}}$ is the number of dual subiterations used at each physical time step to reach the dual steady state, l_{max} is the number of iterations used with the PJ relaxation method, N_{cells} is the grid size and c_u^{BDF} is the unit cost (per point and per iteration) of the PJ–BDF–ALE–AC method. Meanwhile, the global computational cost of the newly proposed TSM approach is expressed as:

$$\mathcal{C}_{\mathrm{TSM}(N)} = (2N + 1) \times m_{\mathrm{max}}^{\mathrm{TSM}(N)} \times l_{\mathrm{max}} \times N_{\mathrm{cells}} \times c_u^{\mathrm{TSM}}(N)$$

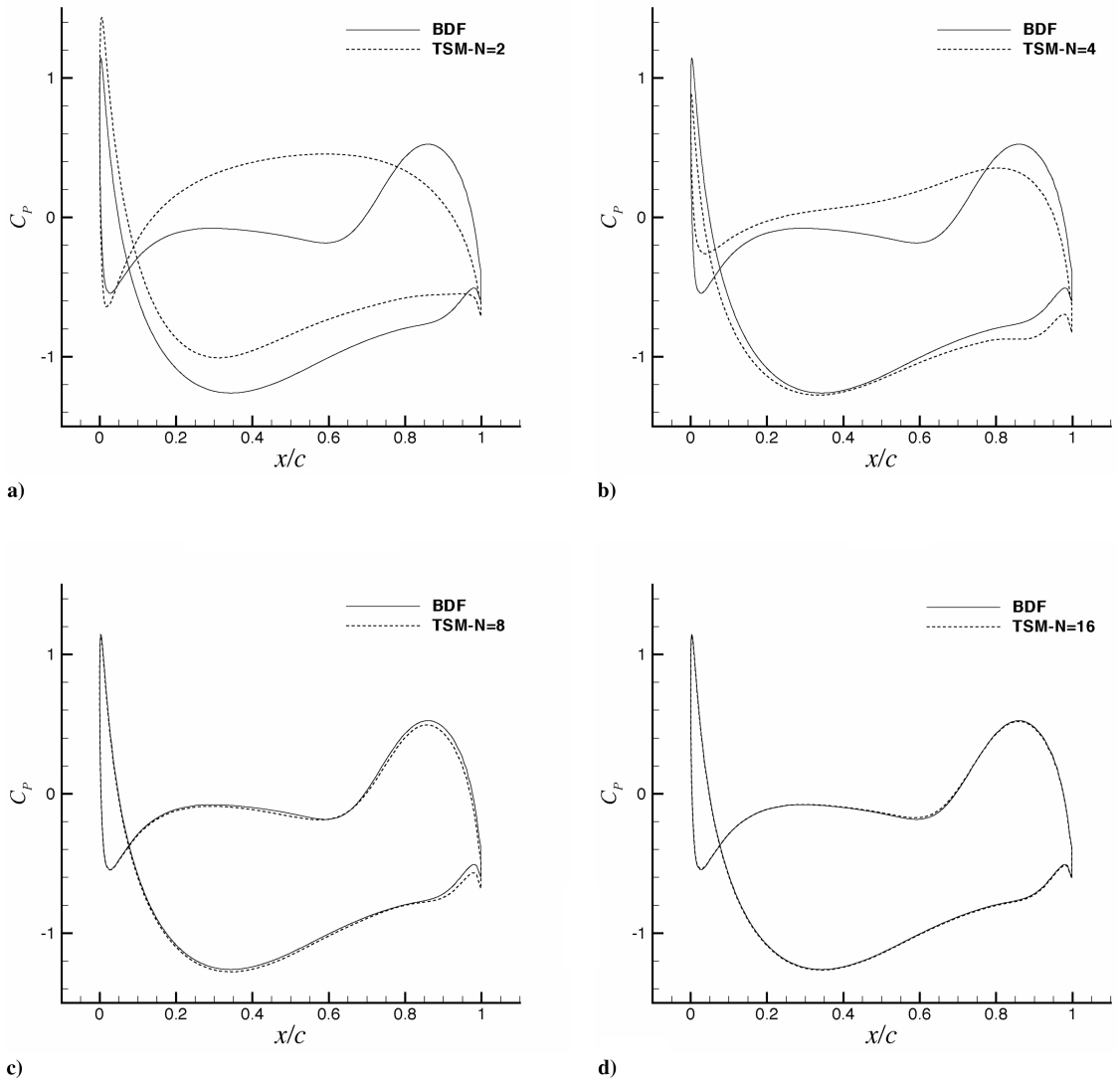

Fig. 9 Flow problem PP. Reconstructed TSM(N) wall pressure coefficient at time $t/T = 0.25$ for an increasing number N of harmonics. Comparison with the reference BDF distribution.

where $(2N + 1)$ is the number of time instances retained to describe the flow period, $m_{\max}^{\mathrm{TSM}}$ is the number of iterations on the dual time needed to drive the PJ–TSM–ALE–AC system to a steady state, $l_{\max}$ is the number of iterations used with the PJ relaxation method, N_{cells} is the grid size and $c_u^{\mathrm{TSM}(N)}$ is the unit cost (per point and per iteration) of this PJ–TSM–ALE–AC method. Since $l_{\max}$ is the same for BDF and TSM, the cost ratio between TSM(N) and BDF used with the same computational grid reads:

$$\eta = \frac{\mathcal{C}_{\mathrm{TSM}(N)}}{\mathcal{C}_{\mathrm{BDF}}} = \underbrace{\frac{(2N+1)}{N_{\Delta t} \times N_{\mathrm{cycles}}} \times \frac{m_{\max}^{\mathrm{TSM}(N)}}{m_{\max}^{\mathrm{BDF}}}}_{\Phi_1} \times \underbrace{\frac{c_u^{\mathrm{TSM}(N)}}{c_u^{\mathrm{BDF}}}}_{\Phi_2}$$

where, for the given flow solver described and used in this work, the contribution Φ_1 depends on the flow problem only while the contribution Φ_2, ratio of the unit costs associated with the TSM(N) and BDF methods, depends on the numerical implementation of these methods into the computer code in use. In the present study, the same number $N_{\Delta t} = 520$ of physical time steps per cycle has been used for PH and PP as well as the same number of dual subiterations $m_{\max}^{\mathrm{BDF}} = 100$. As far as global cost is concerned, and regardless of the accuracy issue for the time being, the PH and PP test cases differ by the number of cycles needed to achieve fully periodic flow ($N_{\mathrm{cycles}}^{\mathrm{PH}} = 6$ while $N_{\mathrm{cycles}}^{\mathrm{PP}} = 4$) and the typical number $m_{\max}^{\mathrm{TSM}(N)}$ of iterations on τ needed to achieve a steady state for the TSM computations. This number is roughly $m_{\max}^{\mathrm{TSM}(N)} \approx 3300$ for PH and $m_{\max}^{\mathrm{TSM}(N)} \approx 2800$ for PP, whatever the number of harmonics N (see Fig. 4). Consequently the global cost ratio for TSM and BDF strategies is given, for test case PH, by

$$\eta^{\mathrm{PH}} = \Phi_1^{\mathrm{PH}}(N) \times \Phi_2(N) = (0.010577 \times (2N+1)) \times \Phi_2(N) \tag{38}$$

and for test case PP by

$$\eta^{\mathrm{PP}} = \Phi_1^{\mathrm{PP}}(N) \times \Phi_2(N) = (0.01346 \times (2N+1)) \times \Phi_2(N) \tag{39}$$

The unit cost ratio between the TSM approach and the BDF method should display a weak dependency only on the number N of harmonics, on one hand through the extra terms introduced by the spectral time approximation and on the other hand through the extra cost that might be induced by the memory access associated with the large-scale TSM systems which couple $2N + 1$ systems of conservation laws. Ideally, with no memory issues, one would expect $\Phi_2(N)$ to remain close to unity whatever the value of N. In practice, the ratio of the TSM(N) and BDF unit costs has been numerically estimated as a linear function of N (which is implementation-dependent)

$$\Phi_2(N) \approx 0.8208 + 0.0925 \times N \tag{40}$$

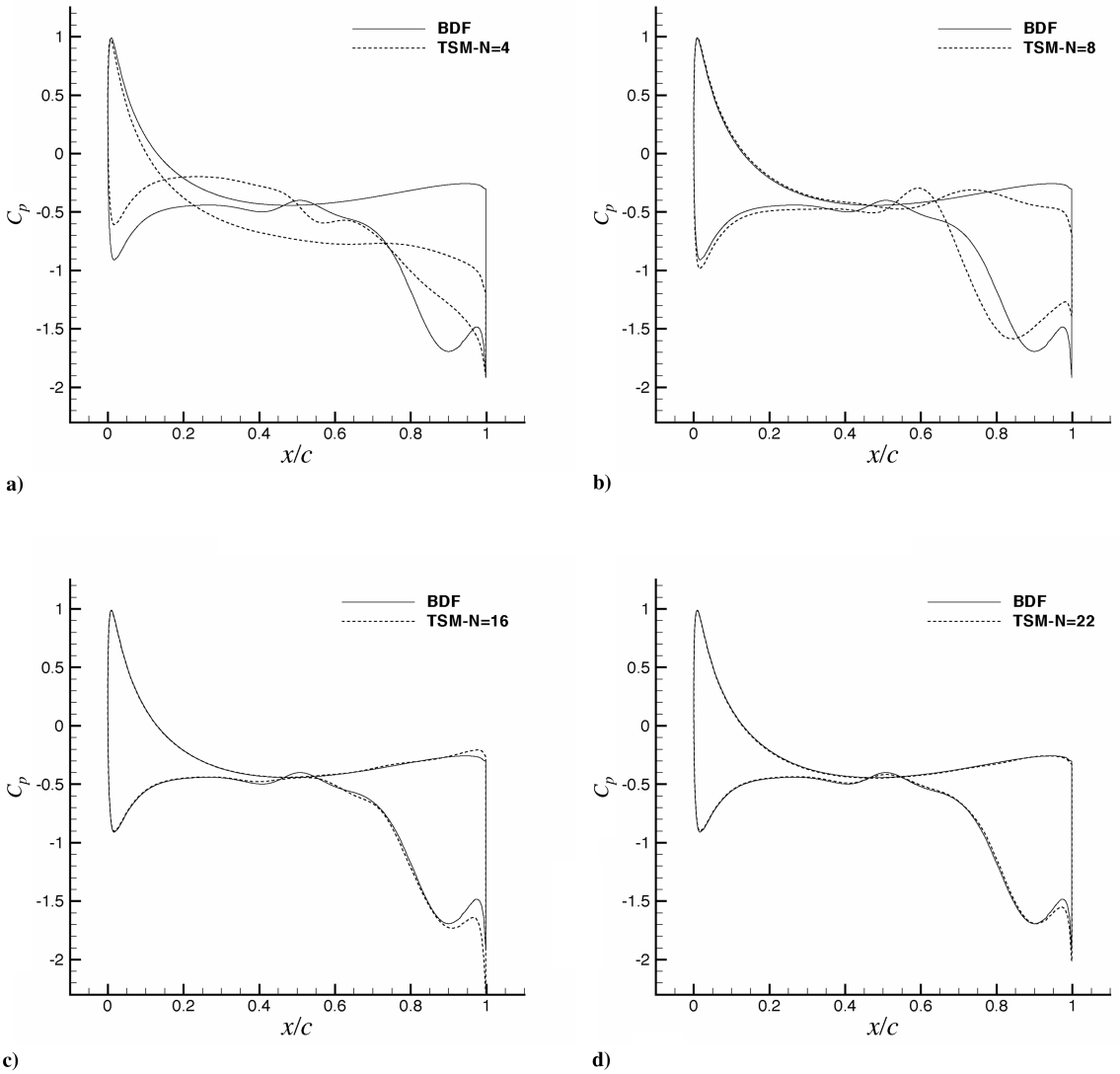

Fig. 10 Flow problem PP. Reconstructed TSM(N) wall pressure coefficient at time $t/T = 0.45$ for an increasing number N of harmonics. Comparison with the reference BDF distribution.

Figure 14 displays the evolution of the global cost ratio for PH and PP, given, respectively, by Eqs. (38) and (39), with the measured unit cost ratio $\Phi_2(N)$ given by Eq. (40), in which case η^{PH} and η^{PP} vary quadratically with N, or with an ideal unit cost ratio roughly equal to 1, in which case the variation of η^{PH} and η^{PP} remains linear with respect to N. Though ideal, this latter case provides an upper limit for the number of harmonics N that might be used by the TSM approach before its computational cost exceeds that of the BDF approach.

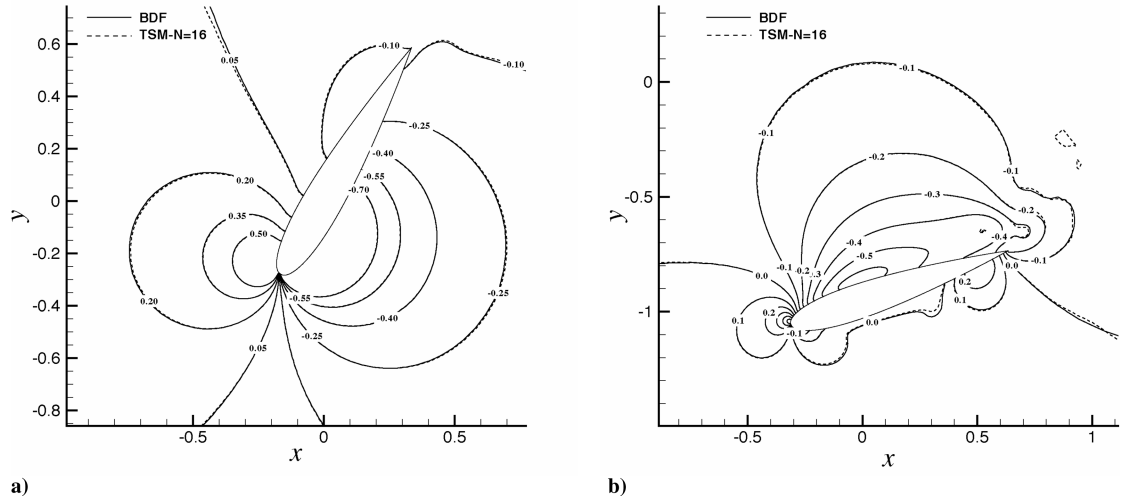

Fig. 11 Flow problem PH. Reconstructed TSM pressure field ($N = 16$) at time a) $t/T = 0.25$ and b) $t/T = 0.45$.

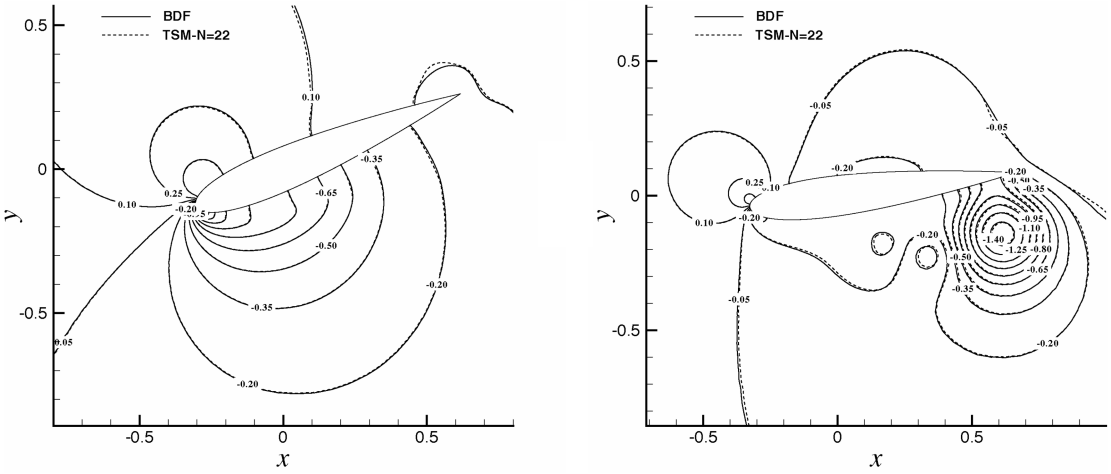

a) b)

Fig. 12 Flow problem PP. Reconstructed TSM pressure field ($N = 22$) at times a) $t/T = 0.25$ and b) $t/T = 0.45$.

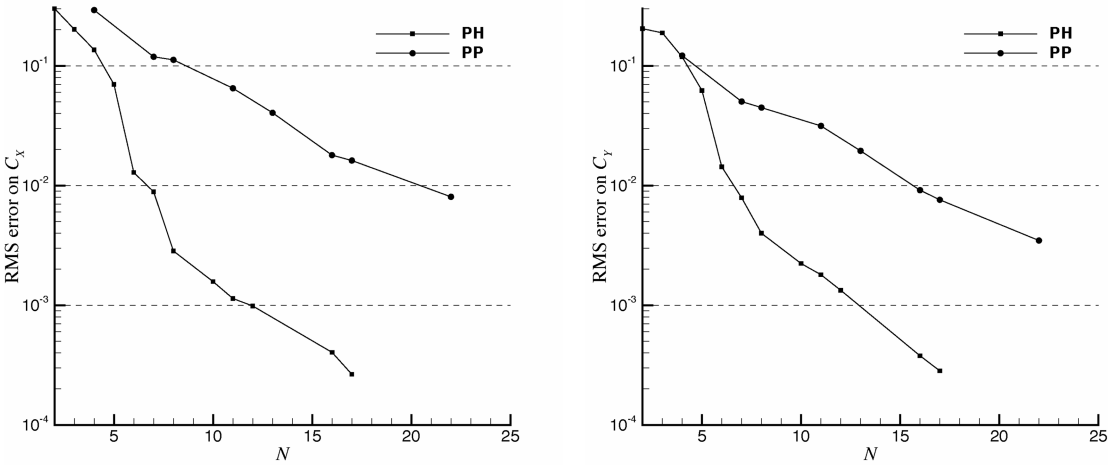

a) b)

Fig. 13 RMS error of the normalized difference between the a) C_X and b) C_Y coefficients computed using the reference BDF strategy with $N_{\Delta t} = 520$ iterations per cycle and the TSM(N) strategy with increasing N.

It can be observed in Fig. 14 that the measured value of η^{PP} reaches 1 for $N = 16$ while η^{PH} remains below 0.8 for this same number of harmonics. With an improved implementation allowing to reduce the growth of the unit cost Φ_2 with N, the global cost ratio η could remain below 0.5 for $N = 16$.

The key point of the present efficiency analysis is reached when crossing the evolution of $\eta(N)$ given by Fig. 14 with the accuracy assessment summarized on the RMS errors for C_X and C_Y plotted in Fig. 13. The RMS errors on these aerodynamic coefficients are plotted against the global efficiency ratio η in Fig. 15: the solid lines correspond to the measured evolution of η^{PH} and η^{PP} while the dashed lines correspond to the ideal evolution where the unit cost ratio Φ_2 would remain roughly equal to 1. From the previously performed accuracy analysis, the BDF and reconstructed TSM solutions were found to be almost coincident when the normalized RMS error on C_Y dropped below 1%, corresponding to a number of harmonics $N = 8$ for the PH case and $N = 16$ for the PP case. Retaining this same criterion, it can be observed in Fig. 15 the TSM approach provides a solution as accurate as the conventional BDF strategy for an overall cost divided by five when computing the PH case; meanwhile, for the PP case, the larger number of harmonics needed by the TSM approach to provide the same level of accuracy as BDF does not allow to reduce the CPU cost, with $\eta^{PP} \approx 1$ for $N = 16$. An improved implementation of the TSM approach could make the

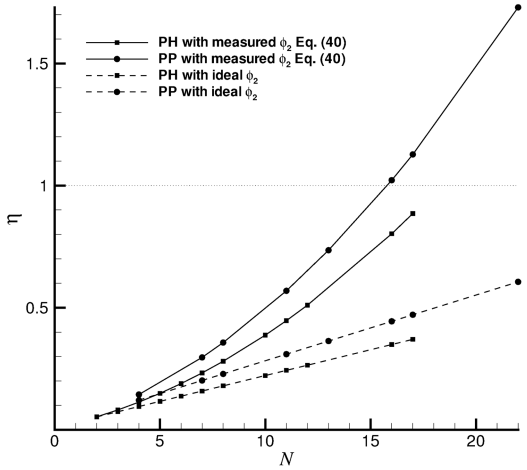

Fig. 14 Evolution of the global cost ratio $\eta = \mathcal{C}_{TSM(N)}/\mathcal{C}_{BDF}$ between TSM(N) and BDF with an increasing number N of harmonics for TSM(N). Solid lines: measured cost ratio for the PH and PP test cases. Dashed lines: ideal cost ratio with a TSM(N) implementation of unit cost Φ_2 roughly equal to the unit cost of the BDF approach.

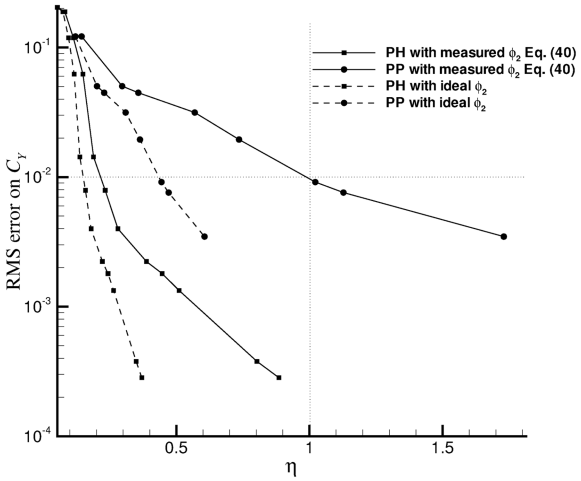

Fig. 15 Evolution of the RMS error on C_Y as a function of the global cost ratio $\eta = \frac{C_{\mathrm{TSM}(N)}}{C_{\mathrm{BDF}}}$ for test problems PH and PP. Solid lines: measured cost ratio. Dashed lines: ideal cost ratio with a TSM(N) implementation of unit cost Φ_2 roughly equal to the unit cost of the BDF approach.

method attractive even for the PP test case, with an ideal computational cost ratio that could go down to 0.5 for $N = 16$ in that case. The analysis of the TSM efficiency has been focused on the achievable CPU gain using the steady computation of a reduced number of modes within a flow period instead of a full unsteady computation over several cycles. It must be pointed out, however, the TSM method is also more demanding memorywise than the BDF strategy since it requires to store $(2N + 1) \times N_{\mathrm{cells}}$ unknown states at each step of the steady-state convergence process against N_{cells} unknown states for the BDF method at each step of the time-marching process.

V. Conclusions

The TSM method has been successfully applied to the computation of periodic incompressible flows over airfoils using an AC formulation within an ALE framework on general unstructured grids. As pointed out by previous authors [6–8], the implicit treatment of the large-scale TSM system, coupling $(2N + 1)$ systems of conservation laws with N the number of harmonics retained to describe the periodic flows under study, is crucial to ensure the efficiency of the TSM method with respect to a conventional BDF formula. In the present work, an implicit formulation of the TSM method has been derived from a simple matrix-free treatment previously developed in the context of compressible flows and readily applicable to the AC system. Special care has been taken to ensure the diagonal dominance property of the TSM implicit stage, with a simple modification of the diagonal contribution which does not significantly affect the convergence of the implicit solver to a steady state. A basic point-relaxation technique has been retained to solve the linear system associated implicit TSM scheme for a very low cost per iteration which makes up for the reduced intrinsic efficiency of the method (a few thousand inexpensive iterations are needed to achieve steady state). The computation of low-Reynolds periodic flow over a pitching and heaving NACA0015 airfoil has demonstrated that between $N = 8$ and $N = 16$ harmonics are required by the TSM method to accurately represent these two-dimensional unsteady flows. This coarse representation of the flow cycle offered by the spectral formula used for discretizing the physical time derivative combined with an efficient solution of the steady solution for the TSM system coupling the $(2N + 1)$ selected unknown fields within a flow period has allowed a substantial gain of CPU time for the computed pitching and heaving test case over a NACA0015 airfoil: a level of accuracy on the flow solution over a period comparable to that offered by a conventional BDF time integration was achieved using an overall CPU time divided by a factor five. Note, however, no reduction was observed using TSM(N) for the pure pitching test case at a lower reduced frequency because twice as many harmonics (16 instead of 8) were needed in that case to achieve an accuracy level similar to that of the BDF approach. To make the TSM approach computationally attractive even when a rather large number of modes are required to achieve a sufficient level of accuracy, ongoing work is devoted on one hand to the optimal implementation of the method so as to reduce as much as possible the growth of the unit cost ratio Φ_2 when N increases and on the other hand to the efficiency improvement of the implicit solver with respect to the PJ method used in the present study in order to potentially reduce both Φ_1 and Φ_2. Efficient relaxation strategies proposed for instance in [33] will be investigated in this perspective. Our current research is also focused on strategies allowing an automatic determination of the number of harmonics to be used with the TSM approach for ensuring a prescribed accuracy level.

References

[1] Peyret, R., and Taylor, T. D., *Computational Methods in Fluid Flow*, 2nd ed., Springer–Verlag, New York, 1983.

[2] Jameson, A., "Time-Dependent Calculations Using Multigrid with Applications to Unsteady Flows Past Airfoils and Wings," 10th AIAA Computational Fluid Dynamics Conference, AIAA Paper 91-1596, June 1991.

[3] Hall, K. C., Thomas, J. P., and Clark, W. S., "Computation of Unsteady Nonlinear Flows in Cascades Using a Harmonic Balance Technique," *AIAA Journal*, Vol. 40, No. 5, 2002, pp. 879–886 .

[4] Gopinath, A., and Jameson, A., "Time Spectral Method for Periodic Unsteady Computations over Two- and Three-Dimensional Bodies," 43rd AIAA Aerospace Sciences Meeting and Exhibit, AIAA Paper 2005-1220, Jan. 2005.

[5] van der Weide, E., Gopinath, A., and Jameson, A., "Turbomachinery Applications with the Time Spectral Method," 35th AIAA Fluid Dynamics Conference and Exhibit, AIAA Paper 2005-4905, June 2005.

[6] Sicot, F., Puigt, G., and Montagnac, M., "Block-Jacobi Implicit Algorithms for the Time Spectral Method," *AIAA Journal*, Vol. 46, No. 12, 2008, pp. 3080–3089.
doi:10.2514/1.36792

[7] Woodgate, M. A., and Badcock, K. J., "Implicit Harmonic Balance Solver for Transonic Flow with Forced Motions," *AIAA Journal*, Vol. 47, No. 4, 2009, pp. 893–901.
doi:10.2514/1.36311

[8] Su, X., and Yuan, X., "Implicit Solution of Time Spectral Method for Periodic Unsteady Flows," *International Journal for Numerical Methods in Fluids*, Vol. 63, Jan. 2009, pp. 860–870.
doi:10.1002/fld.2111

[9] Ekici, K., and Hall, K. C., "Nonlinear Analysis of Unsteady Flows in Multistage Turbomachines Using Harmonic Balance," *AIAA Journal*, Vol. 45, No. 5, 2007, pp. 1047–1057.
doi:10.2514/1.22888

[10] Butsuntorn, N., and Jameson, A., "Time Spectral Method for Rotorcraft Flow," 46th AIAA Aerospace Sciences Meeting and Exhibit, AIAA Paper 2008-403, Jan. 2008.

[11] Antheaume, S., Maître, T., and Achard, J.-L., "Hydraulic Darrieus Turbines Efficiency for Free Fluid Flow Conditions Versus Power Farms Conditions," *Renewable Energy*, Vol. 33, No. 10, 2008, pp. 2186–2198.
doi:10.1016/j.renene.2007.12.022

[12] Amet, E., Maître, T., Pellone, C., and Achard, J.-L., "2D Numerical Simulations of Blade-Vortex Interaction in a Darrieus Turbine," *Journal of Fluids Engineering*, Vol. 131, 2009, pp. 111103.

[13] Jameson, A., "An Assessment of Dual-Time Stepping, Time Spectral and Artificial Compressibility Based Numerical Algorithms for Unsteady Flow with Applications to Flapping Wings," 19th AIAA Computational Fluid Dynamics, AIAA Paper 2009-4273, June 2009.

[14] Kinsey, T., and Dumas, G., "Parametric Study of an Oscillating Airfoil in a Power-Extraction Regime," *AIAA Journal*, Vol. 46, No. 6, 2008, pp. 1318–1330.
doi:10.2514/1.26253

[15] Kloczko, T., Corre, C., and Beccantini, A., "Low-Cost Implicit Schemes for All-Speed Flows on Unstructured Meshes," *International Journal for Numerical Methods in Fluids*, Vol. 58, No. 5, 2008, pp. 493–526.
doi:10.1002/fld.1730

[16] Chorin, A. J., "A Numerical Method for Solving Incompressible Viscous Flow Problems," *Journal of Computational Physics*, Vol. 2, No. 1, 1967, pp. 12–26.

doi:10.1016/0021-9991(67)90037-X
[17] Roe, P. L., "Approximate Riemann Solvers, Parameter Vectors, and Difference Schemes," *Journal of Computational Physics*, Vol. 43, No. 2, 1981, pp. 357–372. doi:10.1016/0021-9991(81)90128-5
[18] Barth, T. J., and Jespersen, D. C., "The Design and Application of Upwind Schemes on Unstructured Meshes," 27th AIAA Aerospace Sciences Meeting, AIAA Paper 89-0366, Jan. 1989.
[19] Delanaye, M., "Polynomial Reconstruction Finite Volume Schemes for the Compressible Euler and Navier–Stokes Equations on Unstructured Adaptive Grids," Ph.D. Thesis, Université de Liège, Belgium, The Netherlands, 1996.
[20] Taylor, L. K., and Whitfield, D. L., "Unsteady Three-Dimensional Incompressible Euler and Navier–Stokes Solver for Stationary and Dynamic Grids," 22nd AIAA Fluid Dynamics, Plasma Dynamics and Lasers Conference, June 1991.
[21] Noh, W., "Cel: A Time-Dependent Two-Space Dimensional Coupled Eulerian-Lagrangian Code," *Methods in Computational Physics*, Vol. 3, 1964, pp. 117–119.
[22] Nakahashi, K., and Deiwert, G. S., "Self Adaptive Grid Method with Application to Airfoil Flow," *AIAA Journal*, Vol. 25, No. 4, 1987, pp. 513–520. doi:10.2514/3.9655
[23] Batina, J. T., "Unsteady Euler Algorithm with Unstructured Dynamic Mesh for Complex-Aircraft Aerodynamic Analysis," *AIAA Journal*, Vol. 29, No. 3, 1991, pp. 327–333. doi:10.2514/3.10583
[24] Luo, H., Baum, J. D., and Lohner, R., "An Accurate, Fast, Matrix-Free Implicit Method for Computing Unsteady Flows on Unstructured Grids," *Computers and Fluids*, Vol. 30, No. 2, 2001, pp. 137–159. doi:10.1016/S0045-7930(00)00011-6
[25] Hassan, O., Sørensen, K. A., Morgan, K., and Weatherill, N. P., "A Method for Time Accurate Turbulent Compressible Fluid Flow Simulation with Moving Boundary Components Employing Local Remeshing," *International Journal for Numerical Methods in Fluids*, Vol. 53, No. 8, 2007, pp. 1243–1266. doi:10.1002/fld.1255
[26] Koobus, B., and Farhat, C., "Second-Order Time-Accurate and Geometrically Conservative Implicit Schemes for Flow Computations on Unstructured Dynamic Meshes," *Computer Methods in Applied Mechanics and Engineering*, Vol. 170, Nos. 1–2, 1999, pp. 103–129. doi:10.1016/S0045-7825(98)00207-2
[27] Benek, J. A., Steger, J. L., and Dougherty, F. C., "A Flexible Grid Embedding Technique with Application to the Euler Equations," AIAA Paper 1983-1944, 1983.
[28] Kannan, R., and Wang, Z. J., "Overset Adaptive Cartesian/Prism Grid Method for Moving Boundary Flow Problems," *AIAA Journal*, Vol. 45, No. 7, 2007, pp. 1774–1779. doi:10.2514/1.24200
[29] Jameson, A., and Yoon, S., "Lower-Upper Implicit Schemes with Multiple Grids for the Euler Equations," *AIAA Journal*, Vol. 25, No. 7, 1987, pp. 929–935. doi:10.2514/3.9724
[30] Luo, H., Baum, J. D., and Lohner, R., "A Fast, Matrix-Free Implicit Method for Compressible Flows on Unstructured Grids," *Journal of Computational Physics*, Vol. 146, No. 2, 1998, pp. 664–690. doi:10.1006/jcph.1998.6076
[31] Shannon, C. E., "Communication in the Presence of Noise," *Proceedings of the Institute of Radio Engineers*, Vol. 37, Jan. 1949, pp. 10–21.
[32] Saad, Y., and Schultz, M., "GMRES: A Generalized Minimal Residual Algorithm for Solving Non-Symmetric Linear Systems," *SIAM Journal on Scientific and Statistical Computing*, Vol. 7, No. 3, July 1986, pp. 856–869.
[33] Liang, C., Kannan, R., and Wang, Z. J., "A p-Multigrid Spectral Difference Method with Explicit and Implicit Smoothers on Unstructured Triangular Grids," *Computers and Fluids*, Vol. 38, No. 2, 2009, pp. 254–265. doi:10.1016/j.compfluid.2008.02.004

Z. Wang
Associate Editor